Modelling the Statistics of Microwave Radar Sea Clutter

Luke Rosenberg*, Simon Watts† and Maria Greco‡,
*Defence Science and Technology Group, Australia, †University College London, UK, ‡University of Pisa, Italy
email: luke.rosenberg@dst.defence.gov.au

***Abstract*—One of the key requirements of a radar system is to detect targets against the background interference. This can be a challenging problem in the maritime domain when the sea moves in a complex manner and the characteristics are time-varying or non-stationary. Understanding the characteristics of sea clutter is therefore essential in developing effective and robust detection schemes. The first part of this tutorial provides details of the relevant statistical models from the literature which are typically used to characterise the sea clutter. Using these models enables us to represent clutter in different environments that may be difficult to observe in trials and to predict the performance of radars over a range of different conditions with more confidence. Future radar systems may well comprise transmitters and receivers which are separated by some distance. Analysis of bistatic sea clutter is therefore covered in the second part of this paper with a focus on how the statistics vary with different bistatic angles. The paper then looks at the application of radar models for clutter simulation and performance prediction for both coherent and non-coherent detection schemes.**

I. Introduction

Understanding radar sea clutter is extremely important in developing useful detection schemes. Unfortunately, this can be difficult as the observed characteristics of sea clutter are dependent on the radar system, the collection geometry and the environmental conditions. Traditional detection schemes work by exploiting models for these statistical characteristics, which may or may not be accurate in reality. The focus of this tutorial paper is to look at these characteristics for both monostatic and bistatic geometries. We then present relevant empirical models and show how they can be used for simulating realistic sea clutter and predicting the performance of detection schemes in different scenarios.

The received radar signal comprises a combination of clutter, noise and target returns with the strength of the sea clutter determined by the radar range equation with the mean normalised backscatter varying with the sea-state, the collection geometry (grazing angle and azimuth angle relative to the wind), the polarisation, bandwidth and the carrier frequency. Section II presents a short introduction to the scattering characteristics of sea clutter along with details of the two key datasets used for examples in this paper.

The clutter will also fluctuate in amplitude which is represented by its distribution or probability density function (PDF). With coarse range resolution, a reasonable model for the in-phase or quadrature sea clutter PDF is the Gaussian distribution [1]. However, as the range resolution becomes finer, the variation of the sea surface becomes better resolved and the effect of breaking waves and other discrete events (sea-spikes) are more pronounced. These returns have a larger magnitude which has led to the development of PDF models with longer 'tails'. There are also a number of white noise sources which could potentially impact the detection performance. However at microwave frequencies, the most dominant source is the thermal noise from the radar receiver itself.

One of the most common formulations for the sea clutter PDF is the compound Gaussian model which comprises a speckle component for modelling the small ripples on top of larger waves [1]. These larger waves are then modelled by a slowly varying texture which can be assumed constant over a typical radar dwell period. The most popular compound model is the K distribution which is characterised by two parameters (shape and scale) which can then be related to variations in the collection geometry and environment (sea-state and swell direction). There are other models which explicitly model sea spikes including the KA and KK distributions, while others such as the Pareto distribution just model the longer tails in the presence of spikes.

In order to characterise the statistics of the interference (clutter + noise), detection schemes need to consider multiple samples in time and / or range. For this reason, understanding the correlation from sample to sample along both of these domains is also important. Along slow-time (pulse-to-pulse), the temporal auto-correlation is often analysed in terms of its frequency domain equivalent, the Doppler spectrum. Further details of these sea clutter characteristics and the relevant statistical models from the literature are given in Section III.

Bistatic radars have received considerable attention over recent years for a number of reasons, including the extra degrees of freedom that can be used to extract information on targets and the covertness of the receive node [2]. However, bistatic measurements are significantly more difficult than monostatic ones as there are more variables which influence the sea clutter statistics. Section IV presents a survey of recent studies into bi-static sea clutter, focussing on how the clutter characteristics vary with bistatic angle.

Methods for accurately simulating sea clutter are then presented in Section V. These can be used to stimulate radar processors during development and testing, generate realistic responses and displays in radar trainers and to evaluate radar detection algorithms. Section VI then looks at how sea clutter models can be used for the prediction of radar performance which is an essential part of the design, development, assessment and marketing of radar systems. As many maritime

radars are starting to exploit coherent processing techniques, both non-coherent and coherent detectors are considered.

II. Sea-clutter characteristics

Sea water has a high dielectric constant and hence absorbs very little radar energy. Moreover, radio frequency energy has very little penetration into the ocean surface. In calm conditions, the ocean surface is flat and radar reflections are highly specular. In this case, most of the transmitted energy is scattered away from the radar transmitter and the measured backscatter levels are low. However, as winds increase and the ocean surface becomes rougher, the backscatter becomes more diffuse and measured backscatter levels increase. The qualitative degree of roughness depends on the radar wavelength with the same ocean surface generating specular reflections at high frequencies (HF) but diffuse reflections at microwave frequencies.

The perturbation theory for electromagnetic scattering was developed by Rice [3] and later applied by Peake [4] to compute the radar cross section of land. Wright [5] then extended this theory to water and classified it as a 'slightly rough' surface. He showed that the scattering elements of primary importance for small grazing angles are capillary or short-gravity waves. Bragg resonance occurs when the distance travelled by the radar waves to successive capillary wave crests is half the radar wavelength. In this case, the reflections add together in phase and resonate to produce strong backscatter. A theoretical backscatter model based on Bragg resonance is presented by Ulaby et al. [6]. They note however, that since their model uses only first order theory, the magnitude of the cross polarised channels is predicted to be zero, which is clearly not realistic.

While the Bragg theory does not always match measured backscatter data well, it does provide some insight into the properties of measured backscatter data. For instance, it is commonly observed that backscatter measured with the vertical polarisation is larger than that measured with the horizontala. Bragg theory explains this difference due to Fresnel reflection coefficients [6] and also proposes a reason for the sinusoidal-like variation in ocean backscatter with azimuth angle.

To extend the first order Bragg scattering theory, two scale composite scattering theories were proposed to divide the rough surface into large and small scale components [7]–[11]. The physical motivation for the model comprises a large scale component which is modelled by geometric or physical optics and a small-scale component described by the existing perturbation theory.

Further analysis of experimental data with higher wind speeds then started to reveal more than one signicant component to the Doppler spectrum. For low sea states, Hicks et al. [12] found that the spectrum had a Gaussian shape which broadened as the wind speed increased and became asymmetrical. Similarly, for high sea states, an extra spectral component due to sea-spray was observed by Money et al. [13]. Wright [7] and later Duncan et al. [14] also found a component which could not easily be explained using the composite scattering theory. This was observed primarily in the horizontal polarisation, at low grazing angles and was strongest in the upwind direction (wind travelling to toward the radar). This specular component is known as a 'sea spike' and may be observed from incipient breaking waves, which also have a distinct Doppler characteristic (see [1] for examples). Breaking waves, together with shadowing from wave fronts and multipath interference, also affect the magnitude of the backscatter at low grazing angles and for both polarisations. While the large magnitude variations appear 'spiky', sea spikes are typically characterised by scattering which can either be short lived (discrete) or persistent and last for seconds.

Lee et al. [15] have reported two possibilities to explain the non-Bragg scattering. This includes a wave which is about to break and has a much longer wavelength than the Bragg resonant wave and a breaking wave which has a long wavelength and large specular return. Other observed characteristics of sea-spikes include a longer range extent which may extend over more than one range cell, different pulse to pulse temporal correlation and distinct Doppler properties.

In the remainder of this section, we describe two key data sets which will be used for many of the examples in this paper. These include the Ingara airborne sea clutter dataset in Section II-A and the NetRAD bistatic sea clutter dataset in Section II-B. Other example datasets include the Canadian IPIX X-band radar [16] and the South African CSIR X-band radar [17].

A. Ingara airborne sea clutter dataset

In many of the examples in this paper we will use sea clutter collected by the Australian Defence Science and Technology Group Ingara radar [18]. The motivation for the Ingara experiments in 2004 and 2006 was to collect sea clutter data covering as wide a parameter space as possible. The airborne X-band radar had a 200 MHz bandwidth centred at 10.1 GHz and a nominal pulse repetition frequency (PRF) of 600 Hz. At a slant range of 3.4 km and with a two-way 3 dB (half-power) azimuth beamwidth of $\theta_{3\text{dB}} = 1^\circ$, the azimuth resolution was approximately 63 m. The sea clutter was collected over twelve days with differing sea-states ranging from calm to very rough. As shown in Fig. 1, the radar platform flew in a circular spotlight collection mode with at least six full orbits around the same patch of ocean to cover a large portion of grazing angles between $15^\circ - 45^\circ$. There was also a range of wind and swell directions which greatly effected the clutter statistics. Both dual and fully polarised data were collected, with horizontal (H) and vertical polarisations (V) transmitted alternatively in the latter case.

An example of the dual polarised backscatter intensity data is presented in Fig. 2 as a range-time intensity image. The data corresponds to an upwind viewing geometry with grazing angles between $30^\circ - 35^\circ$. Fig. 3 then shows the corresponding Doppler spectra from the first 128 pulses. The periodic range varying nature of the intensity and spectra are very evident and consistent with the expected spatial variation of the sea surface wave structure. Note that as the Ingara data was collected in a side looking collection geometry from a moving platform,

the observed Doppler spectrum is broader than what would be observed from a stationary radar.

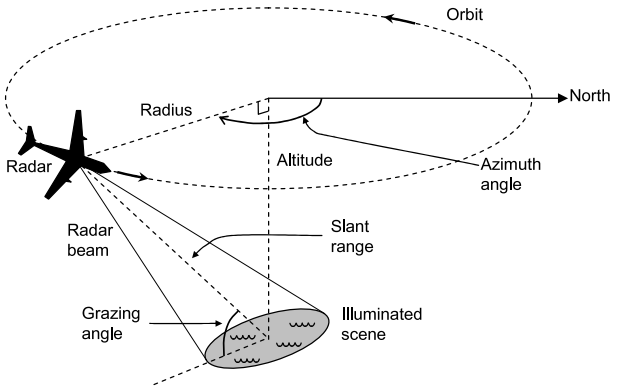

Fig. 1: Ingara circular spotlight collection geometry [19].

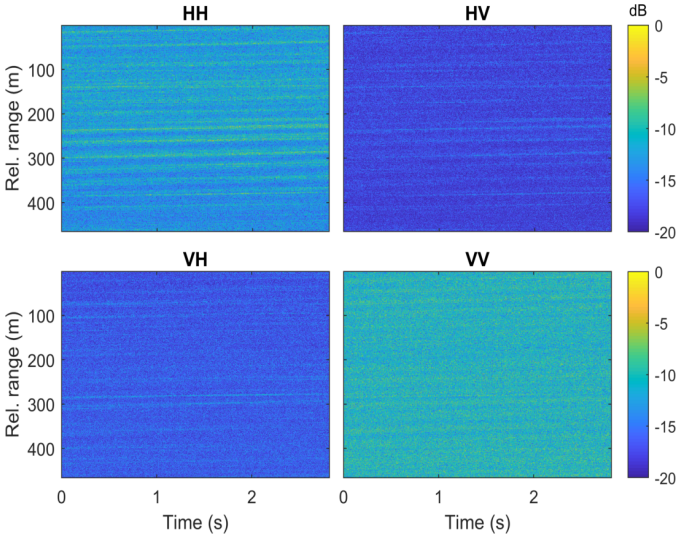

Fig. 2: Time domain intensity image of the Ingara airborne data in the upwind direction.

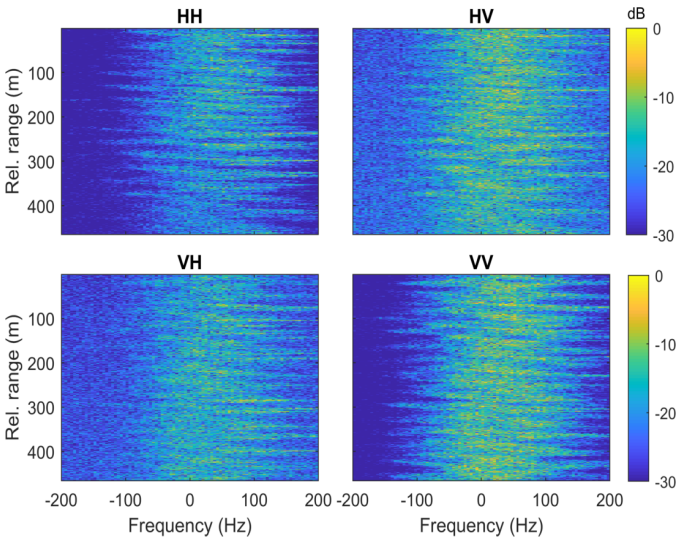

Fig. 3: Doppler spectrum of the Ingara airborne data in the upwind direction.

B. NetRAD bistatic sea clutter dataset

For the bistatic sea clutter analysis, we will use data collected by the S-band ground based netted radar system known as NetRAD [20]. This radar system was jointly developed by the University College London, UK and the University of Capetown, South Africa. It works in both monostatic and bistatic configurations with the two nodes synchronized in time with GPS disciplined oscillators over a 5 GHz wireless link. The monostatic node is composed of a transmitter and a co-located receiver, while the bistatic node operates only as receiver. The transmitted signal has a carrier frequency of 2.4 GHz, a PRF of 1 KHz and a bandwidth of 45 MHz, giving a range resolution of 3.3 m. The antennas work with either vertical or horizontal polarisations and have elevation and azimuth 3 dB beamwidths of $\phi_{3\text{dB}} = 9^\circ$ and $\theta_{3\text{dB}} = 11^\circ$ respectively. They pointed at the sea surface with a grazing angle of 1° and a variable bistatic angle, β.

The radar nodes were placed in an isosceles triangle as shown in Fig. 4, with vertices at the two nodes and the intersection point between their antenna patterns. The effect of this bistatic geometry is that the two-way bistatic range $r_{\text{b}}^{2\text{w}}$ is twice the one way monostatic range $r_{\text{m}}^{1\text{w}}$ and the equivalent one-way bistatic range $r_{\text{m}}^{1\text{w}} = r_{\text{b}}^{2\text{w}}/2$. Hence the clutter power is concentrated in the area illuminated by both the antennas with a range interval $[r_1, r_2]$ given by

$$\begin{aligned} r_1 &= L\cos(\theta_{3\text{dB}}/2)\cos^{-1}(\theta_1 - \theta_{3\text{dB}}/2)\,, \\ r_2 &= L\cos(\theta_{3\text{dB}}/2)\cos^{-1}(\theta_1 + \theta_{3\text{dB}}/2)\,. \end{aligned} \tag{1}$$

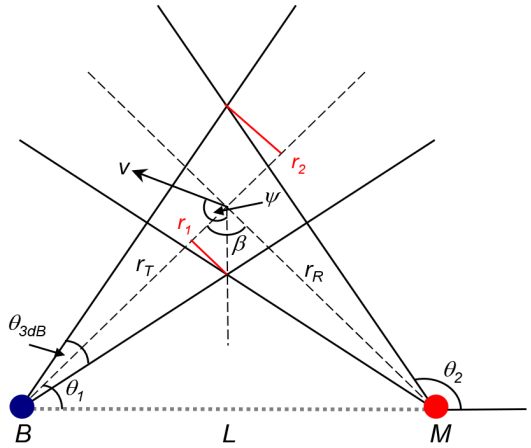

Fig. 4: NetRAD bistatic collection geometry (B: bistatic node, M: monostatic node, L: baseline, β: bistatic angle).

During these collections, the radar was located on a coastal bay facing the Atlantic Ocean, and the wind and wave direction were approximately from the North-West. The weather reports [21] indicated that the wind speed was between 35 km/h to 55 km/h indicating a sea state between 4-5. Figs. 5 and 6 show data collected in October 2010 for the bistatic angle, $\beta = 60^\circ$ with only the common ranges shown as defined in (1).

The bistatic spectra shown on the right side of Fig. 6 show predominately positive Doppler frequency, which is justified

by the fact that the angle formed by the sea waves and the bistatic bisector influences the value of the centre frequency of the bistatic clutter spectrum. If ψ is the aspect angle of the sea waves with respect to the bistatic bisector in the illuminated clutter patch (see Fig. 4), then the bistatic Doppler frequency f_b is given by [22],

$$f_\mathrm{b} = \frac{2v}{\lambda} \cos\psi \cos\frac{\beta}{2} \tag{2}$$

where v is the speed of the sea waves and λ is the radar wavelength.

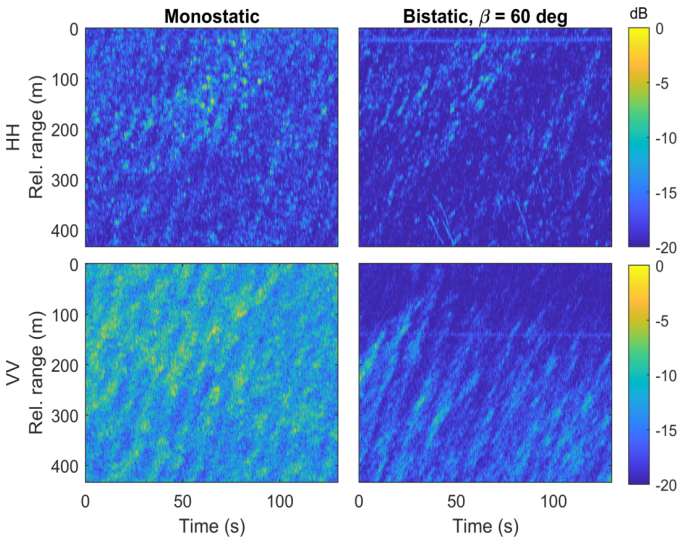

Fig. 5: Time domain intensity image of the NetRAD bistatic data collected at $\beta = 60°$.

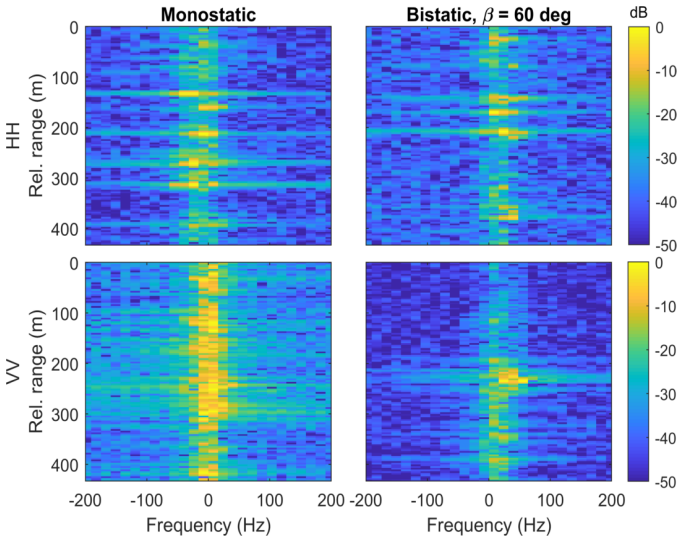

Fig. 6: Doppler spectrum of the NetRAD bistatic data collected at $\beta = 60°$.

III. Sea-clutter models

Understanding the characteristics of sea clutter has been an evolving process since radar was first invented. The most common use of ground and airborne maritime radars is to search for targets at low grazing angles. However, over the past decade, much effort has been invested into understanding the characteristics of sea clutter from higher grazing angles [18], [19], [23]–[32]. This is primarily due to the advent of high flying unmanned aerial vehicles, whose role is to detect targets over large regions of the ocean. In this section, a number of key statistical characteristics are presented for both low and medium grazing angle regions. These include the mean backscatter in Section III-A, the amplitude distribution in Section III-B, texture correlation in Section III-C, sea spikes in Section III-D, the Doppler spectrum in Sections III-E and III-F, and parameter models in Section III-G. There are a number of good reference books in the literature which are relevant to the material presented here. They include Ward Tough and Watts [1], Long [33] and Nathanson [34].

A. Mean backscatter

Modelling the detection performance of a target in clutter requires models for the power of the target, p_s, clutter, p_c, and noise, p_n, with the former two determined by the radar range equation,

$$\begin{aligned} p_\mathrm{s} &= \frac{P_\mathrm{t} G_0^2 \lambda^2 \sigma_\mathrm{t} T_\mathrm{p} B}{(4\pi)^3 R^4 L_\mathrm{a} L_\mathrm{s}}, \\ p_\mathrm{c} &= \frac{P_\mathrm{t} G_0^2 \lambda^2 \sigma_\mathrm{c} T_\mathrm{p} B}{(4\pi)^3 R^4 L_\mathrm{a} L_\mathrm{s}}, \\ p_\mathrm{n} &= k T_0 F_\mathrm{n} B \end{aligned} \tag{3}$$

where P_t is the transmit power, G_0 is the one-way gain on transmit and receive, σ_c and σ_t are the clutter and target radar cross sections (RCS), R is the slant range, L_a and L_s represent the atmospheric and system losses respectively and pulse compression adds a gain given by the pulse length bandwidth product, $T_\mathrm{p}B$. For the noise power, k is Boltzmann's constant, T_0 is the receiver temperature and F_n is the receiver noise figure. The sea clutter RCS, $\sigma_\mathrm{c} = \sigma^0 A_\mathrm{M}$ can be described in terms of the resolution cell area, A_M and the mean backscatter per unit area, σ^0. The resolution cell area for a pulsed radar is defined by the compressed pulse length in range and the antenna beam width in azimuth. A simplified illustration is given in Fig. 7 with the area given approximately by

$$A_\mathrm{M} \approx \alpha_\mathrm{bp} R \theta_\mathrm{3dB} c/(2B) \sec\phi \tag{4}$$

where ϕ is the local grazing angle and c is the speed of light. The factor α_bp in (4) can be used to account for the actual antenna beamshape compared with an idealised rectangular beam. As discussed in [1], $\alpha_\mathrm{bp} = 1$ for a rectangular beam and $\alpha_\mathrm{bp} = 0.75$ for a Gaussian-shaped beam. Correctly modelling the antenna sidelobes is particularly important when assessing the Doppler spectrum of clutter returns from an airborne platform as it will influence the observed Doppler spectrum.

The exact nature of the ocean backscatter depends on the collection geometry as well as the ocean surface roughness and atmospheric effects such as ducting [35]. The latter is often captured by expressing the mean backscatter as $\sigma^0 F^4$, where F is the propagation factor. While this effect can significantly alter the mean backscatter at low grazing angles, it is expected to be less significant as the grazing angle increases. For the

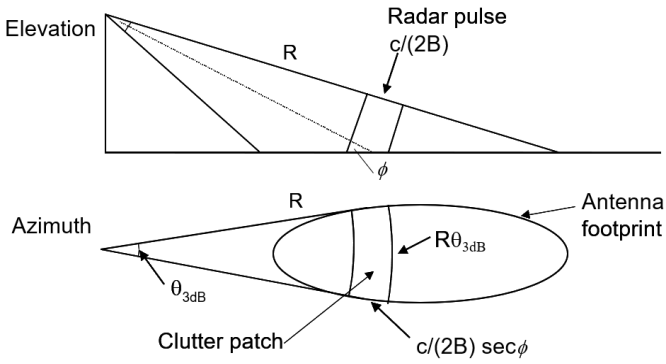

Fig. 7: Clutter patch for a pulsed radar [1].

models presented here, we will not consider it further and this factor is assumed to be unity.

A good starting point for the sea clutter mean backscatter are the tables by Nathanson [36]. These cover a wide range of sea states, grazing angles and radar frequencies but are averaged over all wind directions. The general trends for the mean backscatter as it varies with grazing angle are illustrated in Fig. 8. This shows typical results for σ^0 at X-band, for a wind speed of about 15 kts (7.7 m/s). It can be seen that the HH mean backscatter is generally lower than VV over a range of grazing angles up to 50°. For the first 10°, the low grazing angle or interference region has propagation which is strongly affected by multipath scattering and shadowing from waves. From $10° - 45°$, the mean backscatter is approximately linear and is known as the medium grazing angle or 'plateau' region. Also shown in Fig. 8 is the cross-polarised, VH or HV mean backscatter which is significantly lower than either of the VV or HH values and does not show much variation with grazing angle over the plateau region. A number of models for the mean backscatter have been proposed in the literature and are summarised in Section III-G.

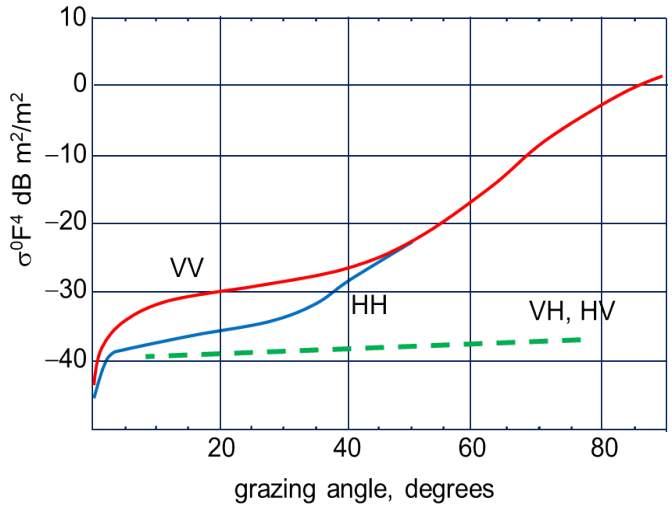

Fig. 8: Mean backscatter variation with grazing angle. Adapted from [1].

B. Amplitude distributions

Detection performance requires an accurate representation of the radar backscatter amplitude or intensity probability density function (PDF). Models for the amplitude distribution of sea clutter are usually developed empirically from measurements of real data as it is not currently possible to accurately predict the PDF of sea clutter under different conditions using physical models of the sea surface. In order to characterise these distributions, it is necessary to estimate the distribution parameters. There are many techniques outlined in the literature including those based on maximum likelihood estimates [37], matching moments of the data with moments of the analytical distributions (method of moments) [1], [37], formulations based on the mean of $z\log z$ [37], [38] and others such as a least squares model fit between the PDF or CDF of the model and the data [23].

There has been a long development of PDF models used to fit both real aperture radar and synthetic aperture radar. Early models include the Rayleigh, log-normal and Weibull, with the latter two distributions used to model the longer tails observed in backscatter due to high magnitude sea spikes [39], [40]. While these have always been present, they were not often observed until the radar resolution became sufficiently fine. A useful distribution family is known as the complex elliptical symmetric distributions [41], [42] which can represent a large number of models including the complex normal, complex-t, generalised Gaussian, Rayleigh, and the compound Gaussian models including the Weibull for some shape values. In the following paragraphs, we summarise the Rayleigh, Weibull, log-normal and generalised Gaussian distributions which are used for the examples in Section IV-B.

Rayleigh: Consider a radar receiving in-phase and quadrature data from an external clutter source with its amplitude defined by Gaussian statistics with zero mean and variance, x. The PDF of the amplitude is then given by a Rayleigh PDF,

$$P(y) = \frac{2y}{x} \exp\left[-\frac{y^2}{x}\right] \tag{5}$$

where the mean, $\langle y \rangle = \sqrt{\pi x}/2$ and the mean square, $\langle y^2 \rangle = x = p_c$ which is the clutter mean power defined in (3). Note that this model is only valid for very coarse resolution sea clutter.

Log-normal: The log normal distribution is typically described in terms of power, $z = y^2$, and arises if we assume the logarithm of z is normally distributed with mean μ and variance δ^2. It is given by [39],

$$P(z) = \frac{1}{z\sqrt{2\pi\delta^2}} \exp\left[-\frac{(\ln z - \mu)^2}{2\delta^2}\right], \quad z \geq 0. \tag{6}$$

Weibull: The Weibull distribution has been used extensively for modelling both land [43] and sea clutter [40]. It is given by

$$P(y) = \frac{c_w}{b_w}\left(\frac{y}{b_w}\right)^{c_w - 1} \exp\left[-\left(\frac{y}{b_w}\right)^{c}_{w}\right], \quad y \geq 0 \tag{7}$$

where $b_w > 0$ and $c_w > 0$ are the scale and shape parameters respectively. The Rayleigh distribution can be obtained by

setting $c_{\rm w} = 2$ with smaller $c_{\rm w}$ implying spikier data. Also for some parameter values, the Weibull distribution is equivalent to the K-distribution and can be considered a compound Gaussian model [44].

***Generalised Gaussian**:* The generalised Gaussian distributions has been used for modelling sea clutter in [45]. It is given by

$$P(y) = \frac{\sigma}{\alpha_{\rm g}\Gamma(\sigma^{-1})s_{\rm g}^{1/\sigma}} \exp\left[-\frac{1}{s_{\rm g}}\left(\frac{y^2}{2\alpha_{\rm g}}\right)^{\sigma}\right], \quad y \geq 0 \tag{8}$$

where $s_{\rm g} = \left[\Gamma(\sigma^{-1})/\Gamma(2\sigma^{-1})\right]^{\sigma}$, $\Gamma(\cdot)$ is the Gamma function, $\alpha_{\rm g} > 0$ is the scale parameter and $\sigma > 0$ is the shape parameter. The Rayleigh distribution is obtained by setting $\sigma = 0.5$ with smaller σ implying spikier data.

A popular and widely used framework for developing PDF models is the compound Gaussian model which was originally proposed for use in sea clutter by Ward [46]. The model comprises a temporal or fast varying component known as speckle which relates to the Bragg scattering, and a slowly varying component which captures the underlying swell and models the texture.

In target detection analysis, the received pulses are often converted to power (square law), $z = y^2$ and the Rayleigh distributed speckle component in (5) becomes exponential,

$$P(z|x) = \frac{1}{x}\exp\left[-\frac{z}{x}\right]. \tag{9}$$

For a frequency agile radar, or a scanning radar with sufficient time between looks, a common method to improve the detection performance is to sum a number of independent non-coherent looks. However, if subsequent pulses are used or the looks are not totally independent, then an 'effective' number of looks will result [47]. Consider the sum of M independent exponential random variables,

$$Z = \sum_{m=1}^{M} z_m. \tag{10}$$

The received power is then described by a gamma PDF,

$$P(Z|x) = \frac{Z^{M-1}}{x^M\Gamma(M)}\exp\left[-\frac{Z}{x}\right]. \tag{11}$$

The distribution in (11) models the speckle component of the sea clutter. For the first order compound Gaussian model, the texture is defined as the speckle mean power and treated as a random variable with a distribution $P(x)$,

$$P(Z) = \int_0^{\infty} P(Z|x)P(x)dx. \tag{12}$$

The extension of this model to a multivariate distribution for the single look vector $\mathbf{z}$ of length $N \times 1$ is a spherically invariant random process, with

$$P(\mathbf{z}) = \int_0^{\infty} \frac{1}{(\pi x)^N|\mathbf{R}|}\exp\left(-\frac{\mathbf{z}^H\mathbf{R}^{-1}\mathbf{z}}{x}\right)P(x)dx \tag{13}$$

where $\mathbf{R}$ is the slow-time covariance of the speckle. One common extension of the compound model is the inclusion of the noise mean power, $p_{\rm n}$. This is achieved by offsetting the variance x in the speckle PDF, giving

$$P(Z|x, p_{\rm n}) = \frac{Z^{M-1}}{(x+p_{\rm n})^M\Gamma(M)}\exp\left[-\frac{Z}{x+p_{\rm n}}\right]. \tag{14}$$

The consequence of this variation is that numerical integration must be used to evaluate (12) and it is no longer possible to use the second order model in (13) to represent the speckle correlation independently of the thermal noise.

The rest of this section outlines a number of compound models which have been used for sea clutter modelling. From these, only the K, KK and Pareto are truly compound Gaussian models.

***K-distribution**:* The most commonly used PDF model for sea clutter in both real and synthetic aperture radar is the K-distribution. To achieve a K-distribution, the texture is gamma distributed

$$P(x) = \frac{b^{\nu}}{\Gamma(\nu)}x^{\nu-1}\exp\left[-bx\right], \qquad \nu, b > 0 \tag{15}$$

with shape given by ν and scale, $b = \nu/p_c$ related to the mean power, p_c. If thermal noise is not present ($p_{\rm n} = 0$), the analytic form of the distribution is given by

$$P(Z) = \frac{2}{Z}(bZ)^{\frac{M+\nu}{2}}\frac{1}{\Gamma(M)\Gamma(\nu)}K_{\nu-M}\left(2\sqrt{bZ}\right) \tag{16}$$

where $K_{\nu-M}(\cdot)$ is the modified Bessel function of the second kind with order $\nu - M$. Commonly in the literature, the noise is not explicitly modelled and the shape is really an 'effective' shape. A key relationship can be derived by matching moments of the PDF with and without noise [1], giving

$$\nu_{\rm eff} = \nu\left(1 + 1/C\right)^2 \tag{17}$$

where C is the clutter to noise ratio (CNR).

***Pareto-distribution**:* The Pareto model is described by two parameters, yet can reasonably model the long tails present in sea clutter distributions. It was first used for sea clutter modelling by Balleri et al. [48], Fayard and Field [40] and later by others at US Naval Research Laboratory (NRL) [49] and DST Group [28], [50].

For the Pareto distribution, the texture has an inverse gamma distribution

$$P(x) = \frac{c^a}{\Gamma(a)}x^{-a-1}\exp\left[-c/x\right], \qquad a > 1, c > 0 \tag{18}$$

where a is the shape and $c = p_c(a-1)$ is the scale. The general solution with no thermal noise is

$$P(Z) = \frac{Z^{M-1}c^a\Gamma(M+a)}{(c+Z)^{M+a}\Gamma(M)\Gamma(a)}, \qquad a > 1, c > 0 \tag{19}$$

which reduces to the generalised Pareto type II or Lomax distribution for $M = 1$,

$$P(Z) = \frac{ac^a}{(c+Z)^{1+a}}. \tag{20}$$

Note that when considering the kth moment for parameter estimation, there is a constraint where $k \geq a$ and hence the mean is undefined for $a \leq 1$ and the second moment for $a \leq 2$. The second moment must be finite if the spatial component

of the clutter results from a wide-sense stationary process. Whether this is always the case for real clutter data is an open question, but we find $a > 2$ for the Ingara data.

There are a number of effective shape parameters derived for this distribution in [28]. Similar to the K-distribution, the relationship based on matching moments is given by

$$a_{\text{eff}} = (a-2)(1+1/C)^2 + 2. \tag{21}$$

KK-distribution: The KK distribution represents a mixture model of two K distributions with the second component designed to model the long tail due to sea-spikes [23], [51]. To implement the KK model, the texture is defined as the sum of two gamma components having shapes, ν_1, ν_2, and scales b_1, b_2. The ratio of the two components is defined by a weighting k_{rat}:

$$P(x) = (1-k_{\text{rat}})P_x(x;\nu_1,b_1) + k_{\text{rat}}P_x(x;\nu_2,b_2) \tag{22}$$

This model can be simplified by equating the two shape parameters and considering the ratio of means as a single parameter. Analysis in [51] found that the ratio of means determined the degree of separation in the tail, while the ratio of the two components determined the point where the tail started diverging.

K+Rayleigh-distribution: Traditionally the dominant Rayleigh component of the received backscatter has been presumed to arise from additive white receiver noise. This case is often referred to in the literature as the K+noise distribution. The K+Rayleigh (K+R) distribution was formalised in [52] after observations by Sletten [53] and Lamont-Smith [54] who found evidence for a further Rayleigh component, beyond what is captured by the thermal noise. It is defined by explicitly separating the speckle mean into two components, $x = x_{\text{r}} + p_{\text{r}}$, where the extra Rayleigh component, p_{r} is modelled in the same fashion as the thermal noise.

The K+R model uses a gamma distribution for the texture,

$$P(x_{\text{r}}|\nu_{\text{r}}, b_{\text{r}}) = \frac{b_{\text{r}}^{\nu_{\text{r}}}}{\Gamma(\nu_{\text{r}})} x_{\text{r}}^{\nu_{\text{r}}-1} \exp\left[-b_{\text{r}}x_{\text{r}}\right], \qquad 0 \le x_{\text{r}} \le \infty \tag{23}$$

where ν_{r} is the shape and $b_{\text{r}} = \nu_{\text{r}}/p_{\text{c}}$ is the scale. To calculate the compound integral in (12), the integration is then performed with the modified speckle mean level, x_{r} instead of the total speckle x. The influence of the extra Rayleigh component can be measured by the ratio of the mean of the Rayleigh component to the mean of the gamma distributed component of the clutter and is defined by $k_{\text{r}} = p_{\text{r}}/p_{\text{c}}$. For the Ingara data, it has typical values in the range $0 \le k_{\text{r}} \le 4$.

KA-distribution: The KA model was originally proposed in [55] and then applied to sea clutter by Ward et al. [1], [56], [57]. A comparison of this model and the KK distribution has been applied to the Ingara data in [51].

The KA distribution represents a mixture of K and a spike component. Each component of the mixture model is functionally identical to the previously discussed K+Rayleigh model, where the Rayleigh component power is now assumed to arise due to the presence of one or more Rayleigh distributed spikes. The probability of a spike being present, $P_M(m)$, is modelled by Poisson statistics which gives a weighting or prior probability for each mixture component. The single look KA distribution can be written as a compound distribution with the following components:

$$\begin{aligned} P(z|x) &= \sum_{m=0}^{\infty} \frac{\exp(-bx)\exp(-z/(x+p_{\text{n}}+m\sigma_{\text{sp}}))P(m)}{x+p_{\text{n}}+m\sigma_{\text{sp}}} \\ P(x) &= \frac{x^{\beta_0-1}\exp(-\beta_0 x/\sigma_{\text{W}})}{\Gamma(\nu)}\left(\frac{\beta_0}{\sigma_{\text{W}}}\right), \end{aligned} \tag{24}$$

where σ_{sp} is the sea-spike intensity, σ_{W} is the mean power of the whitecap component and β_0 is the shape parameter. Note the summation in (24) corresponds to the sum of mixture component probabilities which is typically small and can be truncated at $m = 1$. The Poisson component can be described by

$$P(m) = \exp\left(-\bar{M}\right)\frac{\bar{M}^m}{m!} \tag{25}$$

where $\bar{M}$ is the mean number of spikes in each range cell.

Example fits: In the following example in Figs. 9 and 10, a block of data has been selected from the Ingara dataset over a 5° span of azimuth angles in the upwind direction and a 3° span of grazing angles centred at 30°. This relates to data covering 3.4 second in slow time and 300 m in slant range. Before forming a histogram, the intensity data is vectorised, normalised to ensure unity mean power and converted to decibels (dBs) due to its wide dynamic range. Then a reasonable choice of intensity values are $0 \le z \le 50$ dB. The PDF is then just the histogram normalised to have area 1 and the CDF is formed by a cumulative summation across the intensity values, followed by a normalisation so the maximum value is 1.

The model fits are often represented by the logarithm of the complementary cumulative distribution function (CCDF=1-CDF) as it highlights the tail of the distribution. For the horizontally polarised data in Fig. 9, the top plot shows the exponential, K and K+R distributions with a large mismatch for the first two models. The bottom plot shows similar fits for the Pareto, KK and KA distributions. These latter two generally have a better fit due to the larger number of parameters used for the model fit. For the vertically polarised data in Fig. 10, the data is less spiky and all the models fit the data well except for the exponential distribution.

C. Texture correlation

The correlation of the texture can be characterised by two distinct components. The first is a correlation over a time period on the order of seconds, while the second component is along the range direction and is commonly referred to as spatial correlation. These are typically considered independently as characterisation of the two-dimensional texture is difficult and may not be necessary for short time periods or short range extents. It is also difficult for airborne platforms to characterise the temporal component unless the radar is ground stabilised. An example of a temporal correlation is shown in Fig. 11 for the CSIR data set [17]. This view of the data highlights the non-stationarity of the sea clutter as the correlation does not decay to zero.

To obtain a useful estimate of the spatial correlation, the intensity must be averaged to avoid the impact of speckle

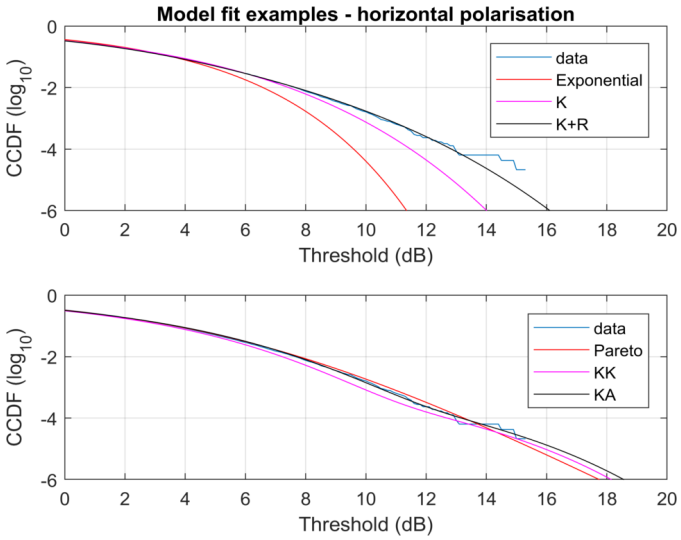

Fig. 9: Example CCDF fits for horizontally polarised Ingara data in the upwind direction and 30° grazing.

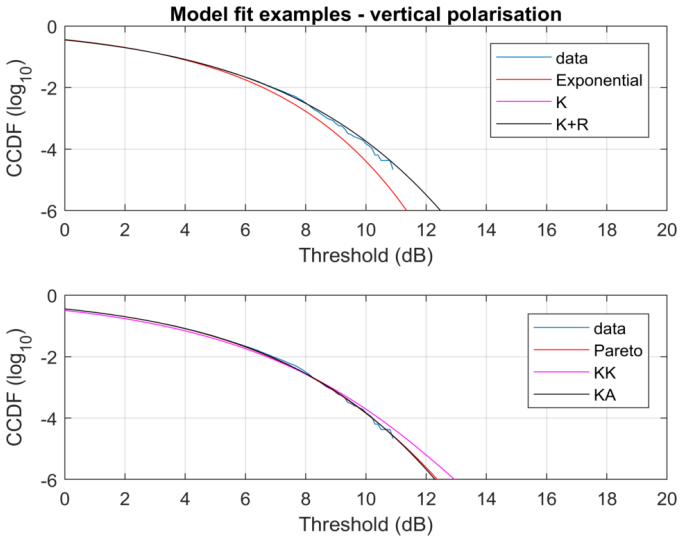

Fig. 10: Example CCDF fits for vertical polarised Ingara data in the upwind direction and 30° grazing.

either along range or slow-time. Fig. 12 shows the two-sided spatial correlation for the VV polarisation of the IPIX ground based radar [58]. The data has been averaged over 128 pulses and processed for three different range resolutions, 3 m, 9 m and 15 m. This result highlights that it is possible to resolve different periodicities by processing the data at finer resolutions. Fig. 13 then shows the spatial correlation of the Ingara dataset averaged over 2 s. The result shows an initial decay and a number of sinusoidal components due to the interaction of the waves.

D. Sea spikes

To better understand the behaviour of the sea spike components, it is useful to isolate them from the sea clutter return. There are three main methods of characterising the sea-spike component of the sea clutter. The first two methods fit relevant

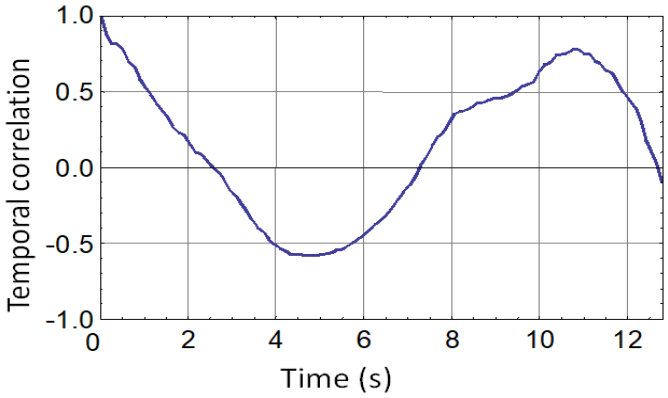

Fig. 11: Temporal correlation for the CSIR data [1].

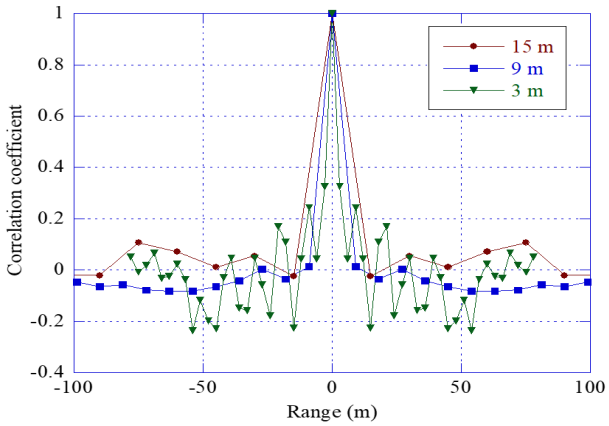

Fig. 12: Spatial correlation for the IPIX data, VV polarisation with different spatial resolutions [58].

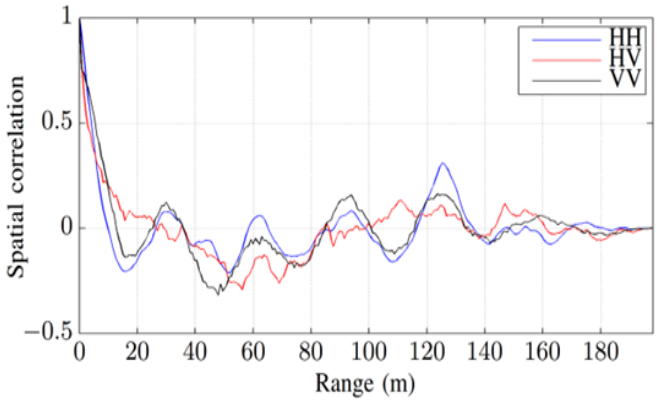

Fig. 13: Spatial correlation example from the Ingara data.

models to the PDF and the mean Doppler spectrum respectively, [23], [51], [59]–[61]. The third method does not assume any underlying statistical model, but involves thresholding the magnitude of the data in order to distinguish between Bragg scattering and sea-spike events [62]–[66]. There are often secondary criteria imposed at this stage such as the spike width and / or the interval between spikes.

An example of the third method has been presented in [24] for the Ingara dataset. The approach taken is to threshold

the magnitude of the raw backscatter data in the range/time domain at 3 standard deviations above the mean. The percentage of sea-spikes present in the data was then measured. The results showed that the majority occur in the lower grazing angle region for the HH channel and are slightly higher in the cross wind directions for the HV and VV channels. These results were verified by comparing the trends with a separate analysis using the KK PDF to model the sea clutter. An image processing algorithm was then used to isolate the short lived (discrete) and long lived (persistent) scatterers which are attributed to whitecaps and lasted for at least 1 s. The results in Figs. 14 and 15 revealed that the persistent whitecaps are spread quite evenly in grazing and azimuth for the HH channel with a clear trend in the cross-wind directions for the HV and VV channels. Based on this information, the wave velocity, life time and spike decorrelation time of the whitecaps were able to be measured and are shown in Fig. 16.

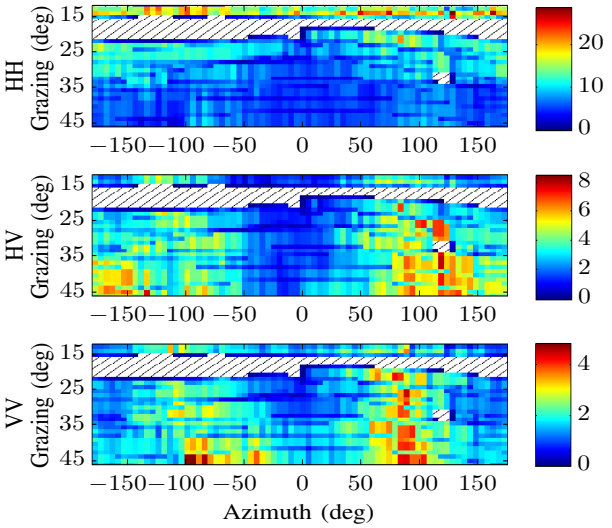

Fig. 14: Percentage of discrete sea-spike detections for the Ingara dataset [24].

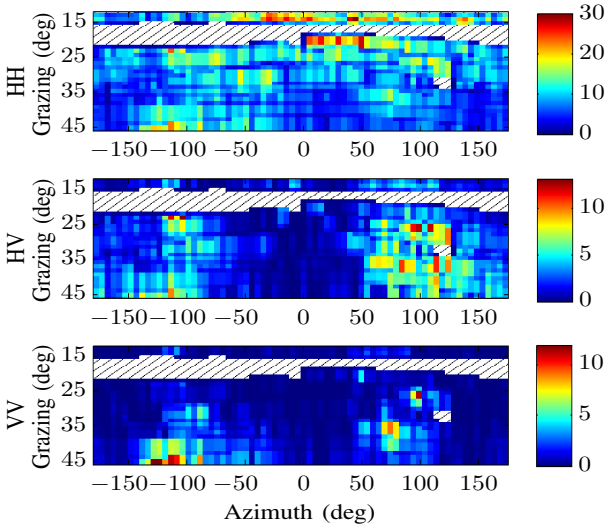

Fig. 15: Percentage of whitecap detections for the Ingara dataset [24].

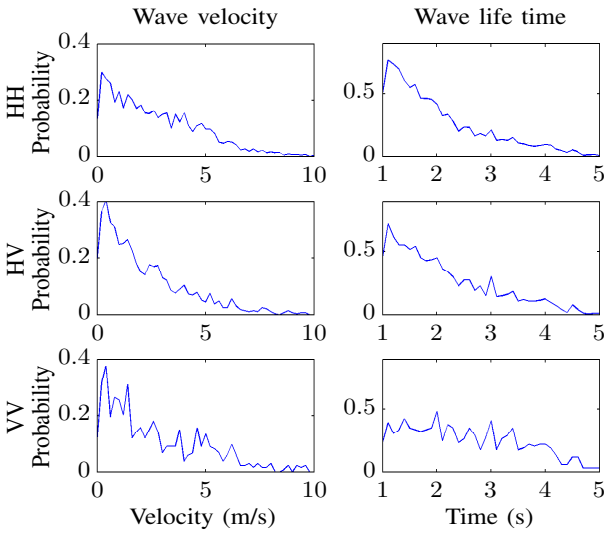

Fig. 16: Sea-spike characteristic PDFs for the Ingara dataset - wave velocity and life time [24].

E. Doppler spectrum

The Doppler spectrum plays an important role in understanding the characteristics of sea clutter. In a non-coherent detection scheme, it determines the amount of pulse to pulse correlation, while for a coherent scheme it plays a more significant role. In the literature, the mean Doppler spectrum is often characterised by a single Gaussian component with an offset and spread [12], [34], [67]. This is in contrast to the asymmetrical spectra which is often observed due to the interplay of both fast and slow scattering mechanisms [1]. As discussed previously, the slow scattering response is primarily associated with resonant Bragg scattering from wind induced capillary wave structures on the sea surface and exhibits Doppler shifts on the order of tens of Hertz (for X-band systems), consistent with the anticipated phase velocity of capillary waves. While the Bragg scattering response typically dominates for vertically polarised radar systems, studies of low grazing angle data have shown that horizontal polarised systems can be heavily affected by fast scattering mechanisms, so named for the higher Doppler frequencies they exhibit in comparison with Bragg scattering.

One of the first bimodal models for low grazing angles was proposed by Lee et al. [68] and comprises two components, a Gaussian for the Bragg scatterers and a Lorentzian and/or Voigtian for the non-Bragg component. The model describes the Doppler spectrum with a good degree of accuracy, but is complicated to understand and interpret. Fig. 17 shows a vertically polarised example from a wavetank where the two components can clearly be seen [68]. A similar model was used by Lamont-Smith [69] who looked at the effect of varying the grazing angle with data collected from both a large wave tank and from a cliff top. His model uses a single Gaussian to represent the slow Doppler component which dominates the vertical channel, and two Gaussian components to represent the slow and fast components in the horizontal channel. This

also corresponds with later observations by Melville, et al. [70] who found that the non-Bragg term was virtually absent in their vertical channel data.

Many authors investigating sea-spikes observed that there is a degree of polarisation independence in the non-Bragg component when looking at sea clutter backscatter. Jessup et al. [62] observed that as the grazing angle increased, the polarisation ratio (HH/VV) which is typically less than one, now approached unity. This influenced the model presented by Walker [59] which uses a combination of three Gaussian components to describe the Doppler spectrum. This included components to model the Bragg scatterers, the persistent polarisation independent return from the breaking waves (white-caps) and the discrete short lived spikes.

At medium grazing angles, Stacy et al. [71] and subsequently Rosenberg et al. [60], [61] reported on Doppler spectra measured from the Ingara data. They fitted the observed spectra to the Walker model with good agreement. However further investigations [24] found that the Walker model did not totally describe the scattering and a modification was required. Consequently, a new two component Doppler spectrum model was introduced in [19] using the Gaussian building blocks that both Walker [59] and Lamont-Smith [69] used.

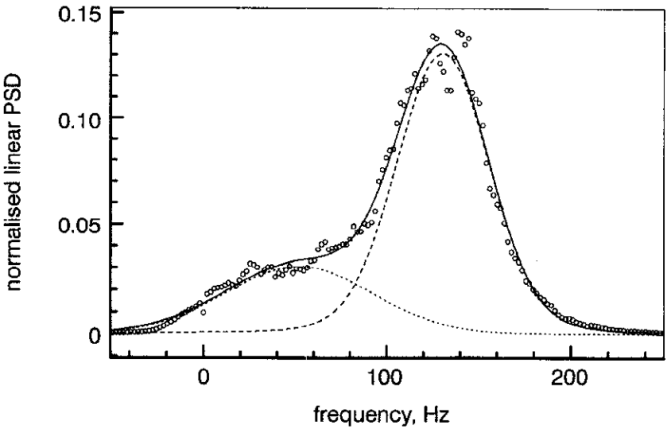

Fig. 17: Mean Doppler spectrum example from a wavetank for vertically polarised data at 7° grazing with: (○) data, (- -) Voigtian component, (· · ·) Gaussian component and (—) combined mean spectrum [68].

F. Evolving Doppler model

While the previous Doppler models are useful to capture the overall mean, the Doppler spectrum actually evolves in both range and time. This evolution in range can be seen in Fig. 3 for the Ingara data, while an example of the time evolution from the IPIX dataset is shown as a spectrogram in Fig. 18. Therefore it is important to correctly model this effect to achieve realistic simulation of sea clutter and accurately determine the detection performance of a coherent radar.

There are only a few models which can model the time and range-varying characteristics of the Doppler spectra. These include the auto-regressive model by Greco et al. [16], the range / time evolution model by Watts [72] and those by Davidson [73] and McDonald and Cerutti-Maori [32].

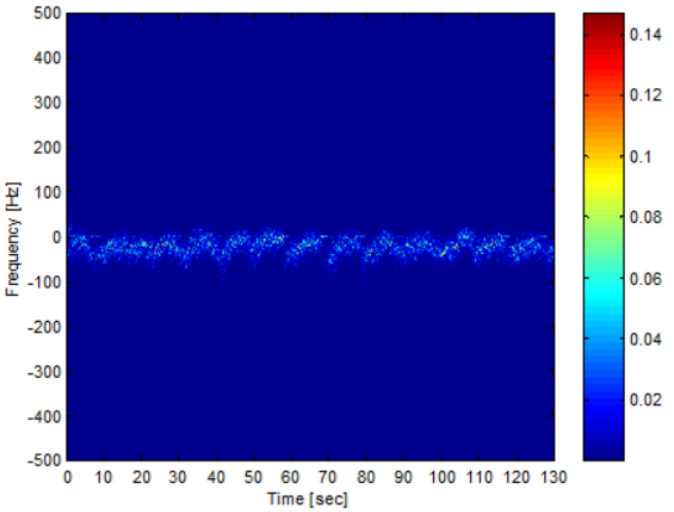

Fig. 18: Normalised spectrogram of the IPIX data showing the time varying spectrum [16].

In this section, we now present the Watts model in further detail. This model has been verified with the CSIR dataset [74], the NetRAD dataset [75] and the Ingara dataset in [27], [76]. It has the following components:

- A model for the texture PDF, correlated over time or range with mean intensity, x. This has previously been modelled as a gamma distribution in [72] and inverse gamma distribution in [77], resulting in compound K and Pareto distributions respectively.
- A Gaussian-shaped spectrum

$$G(f,x,s) = \frac{x}{\sqrt{2\pi}s}\exp\left[-\frac{(f-m_{\mathrm{f}}(x))^2}{2s^2}\right] \tag{26}$$

  where s is the spectrum width and $m_{\mathrm{f}}(x)$ is the mean Doppler frequency.
- The mean Doppler is related to the normalised mean intensity:

$$m_f(x) = A + B\frac{x}{\langle x\rangle} \tag{27}$$

- A PDF for the spectrum width, s with mean, m_s and variance, σ_s^2. The original work in [72] proposed a Gaussian PDF although a gamma PDF should fit equally well for parameter values encountered in practice.

This model has been extended for multiple phase centres in [78] and for a multiple phase centre scanning radar in [79]. It was also observed for the Ingara data that at high values of normalised intensity, the rate of increase of $m_{\mathrm{f}}(x)$ with x appeared to reduce when looking up or downwind. In [76], this observation was explained as an increasing bimodal behaviour above some level of intensity.

A possible general model for the clutter power spectrum was given by a mixture model of two Gaussian-shaped power

spectra:

$$G(f,x,s_1,s_2) = \frac{\alpha x}{\sqrt{2\pi}s_1}\exp\left[-\frac{(f-m_{\mathrm{f}_1}(x))^2}{2s_1^2}\right] + \frac{(1-\alpha)x}{\sqrt{2\pi}s_2}\exp\left[-\frac{(f-m_{\mathrm{f}_2}(x))^2}{2s_2^2}\right] \quad (28)$$

where

$$\begin{aligned} m_{\mathrm{f}_1}(x) &= A + Bx, \quad x \le t_{\mathrm{bi}} \\ &= A + Bt_{\mathrm{bi}}, \quad x > t_{\mathrm{bi}} \\ m_{\mathrm{f}_2}(x) &= A + Bx. \end{aligned} \quad (29)$$

This has the effect of broadening the spectrum if x exceeds some threshold, t_{bi}. Such bimodal behaviour will be reflected in estimates of the mean Doppler shift and variance of the total spectrum. Fig. 19 shows an example of the bimodal fit of the Ingara data from [27], where the HH upwind result clearly has two components, while the VV upwind and all crosswind results are more linear.

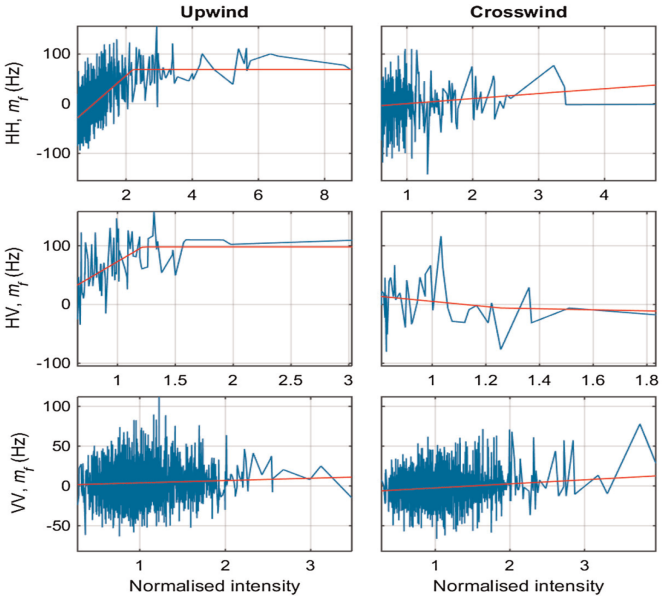

Fig. 19: Spectrum mean of the Ingara data as a function of intensity. Blue is the measured data and red is the bimodal model fit [27].

G. Parameter models

Practical use of these statistical models requires a way to relate the model parameters to the sea conditions, collection geometry, polarisation and frequency. This can be done either empirically based on measured data or with physical based electromagnetic modelling [1], [31], [80]. In general, these latter approaches are too computationally intensive to be used for most applications and are not described further here.

Many empirical models for the mean backscatter are based on fits to Nathanson's tables [36] with some adding a variation to account for changes in the wind direction. These cover a range of frequencies and geometric and environmental conditions. They include the Technology Services Corporation (TSC) [35], NATO Anti Air Warfare Systems (NAAWS) [81], Hybrid [82] and Naval Research Laboratory (NRL) [83] models. A second group of mean backscatter models are designed to fit the relationships described by Ulaby et al. [6]. These are the Masuko [84] and Ingara Imaging Radar Systems Group (IRSG) linear [85] models. One final mean backscatter model which is widely used in the literature is from the Georgia Institute of Technology (GIT) [86] and covers $0.1^\circ - 10^\circ$ grazing, all azimuth angles, a range of wind speeds from $3-30$ kts ($1.5-15.4$ m/s), frequencies from $1-100$ GHz and both horizontal and vertical polarisations. Figs. 20 and 21 shows slices through many of these models along both grazing and wind speed for the horizontal polarisation and upwind direction. For the first plot, the wind speed is fixed at 9.4 m/s, while for the second, the grazing angle is fixed at 30°.

TABLE I: Summary of mean backscatter models. Note all models are valid for both HH and VV polarisations.

Model	Frequency (GHz)	Grazing angle (°)	Azimuth angle (°)	Sea state
TSC	0.5-35	0-90	0-360	0-5
NAAWS	0.5-70	0-30	0-360	3-6
NRL	0.5-40	0.1-60	averaged	0-6
MASUKO	10, 34	0-70	0-360	2-6
IRSG	10.1	20-45	0-360	2-6
GIT	1-100	0.1-10	0-360	0.4-7.1
DST Continuous	10.1	0.1-45	0-360	2-6

While a number of the models described here cover grazing angles above 10°, they have shown to be a poor fit to the Ingara medium grazing angle data set [85]. Most are designed for either low gazing angles (typically less than 10°) or medium grazing angles (greater than 15°) and cannot be used continuously when modelling radar performance or simulating sea clutter for geometries that span both the low and medium grazing angle regions. To address this problem, the DST continuous model was developed in [87] covering 0.1° - 45° grazing and combining the GIT model at low grazing angles and a fit to the Ingara data for medium grazing angles. This model covers both horizontal and vertical polarisations, any wind direction and sea states $1-6$. Table I summarises the mean backscatter models presented here where the sea state, $\tilde{S}$ is used to represent the sea condition. To convert between wind speed U and sea state, the following relationship is used, $U = 3.2\tilde{S}^{0.8}$ [35].

An example is shown in Fig. 22 with the data on the left and the model fit on right. The data comprises an instantiation of the GIT model for grazing angles $0.1^\circ - 10^\circ$ and the Ingara data from $15^\circ - 45^\circ$.

The K-distribution is the most common amplitude distribution model for representing the fluctuation of sea clutter. At low grazing angles ($< 10^\circ$), there are a few models for the K-distribution shape, ν, based on a dataset summarised in [1]. This includes the original shape model presented by Ward [88] and the updated fits by Watts and Wicks [89]. At medium grazing angles, there are a number of models based on the Ingara medium grazing angle data set. The first was designed to model only the geometry for an individual day [90]. This was then extended by Crisp et al. [91] and then Rosenberg et al. [76] to include extra components for the environmental

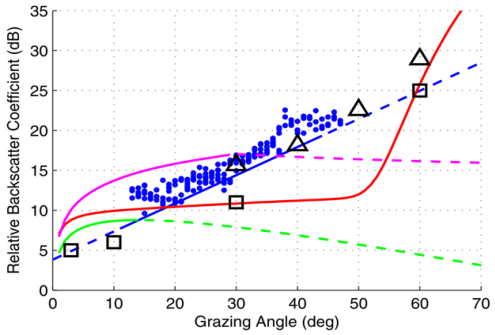

Fig. 20: Relative mean backscatter variation with grazing angle. Data is from the horizontal polarisation, 9.4 m/s wind speed and upwind [85]. Dashed lines indicate regions where the models are not valid. Models / data represented include: blue - IRSG linear, magenta - NAAWS, red - TSC, green - GIT, △ - Masuko, □ - Nathanson, • Ingara data.

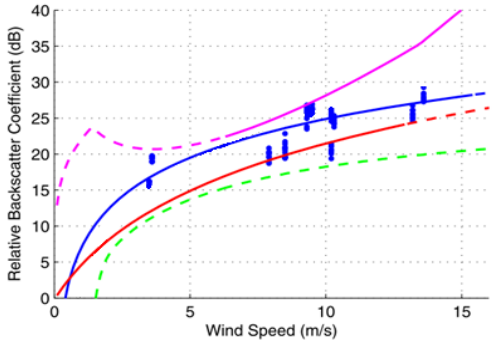

Fig. 21: Relative mean backscatter variation with wind speed. Data is from the horizontal polarisation, 30° grazing and upwind [85]. Dashed lines indicate regions where the models are not valid. Models / data represented include: blue - IRSG linear, magenta - NAAWS, red - TSC, green - GIT, • Ingara data.

conditions and resolution cell area. Finally, a continuous model over the grazing angle range $0.1° - 45°$ was presented in [87] using a modified version of the Watts and Wicks model to cover all swell directions combined with the medium grazing angle model from [76]. Fig. 23 shows the data on the left and an example model fit on the right for a resolution cell area $A_c = 756$ m^2. The data comprises an instantiation of the modified Watts and Wicks model for grazing angles $0.1° - 10°$ and the Ingara data from $15° - 45°$.

There are very few models for the Doppler spectrum, given the difficulty in modelling its time and range varying nature. Many are based on a single Gaussian model for representing the mean spectrum such as the one by Wetzel [67]. This model is based on low grazing angle data in the upwind direction and relates the mean velocity of the Doppler spectrum to the wind speed:

$$\begin{aligned} V_{\text{HH}} &= 0.25 + 0.25U, \\ V_{\text{VV}} &= 0.25 + 0.18U, \end{aligned} \tag{30}$$

where V_{VV} and V_{HH} denote the velocities of the vertical and horizontal polarisations respectively. The half-power width is quite variable but is given approximately by $\Delta = 0.24U$.

At medium grazing angles, a parametric model for the parameters of the evolving Doppler model was given in [92] and later extended for the bimodal case in [76]. This model is based on the data at the finest resolution cell area of the Ingara data, 0.75×63 m^2 and includes both the wind and swell directions.

Due to the non-stationarity of sea clutter, it is difficult to model the spatial correlation of sea clutter. This is shown in Fig. 13 which highlights the variability in the autocorrelation. As a result, it is typically characterised by the length of the initial decay, r_{c} measured at the point where the normalised correlation reaches $1/e \approx 0.37$. Using this value, either a negative exponential or Gaussian function can be used to model the correlation. An example of the latter is given by

$$R_{\text{spat}}(y) = \exp\left[-\frac{y^2}{r_{\text{c}}^2}\right]. \tag{31}$$

At low grazing angles, a suitable model for the spatial decorrelation length is presented in [93],

$$r_{\text{c}} = \frac{\pi U^2}{2g}\sqrt{3\cos^2\theta + 1} \tag{32}$$

where $g \approx 9.81$ m/s^2 is the gravitational acceleration and θ is the azimuth wind direction with respect to the radar line of sight. For medium grazing angles, the model in [76] can be used.

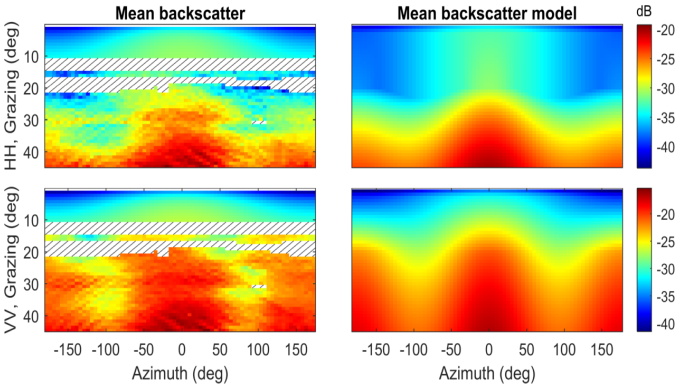

Fig. 22: Mean backscatter - data on left and model fit on right. Data comprises the GIT model for grazing angles $0.1° - 10°$ and the Ingara data from $15° - 45°$ [87].

IV. Bistatic Clutter Analysis and Modelling

Bistatic radars offer extra degrees of freedom that can be utilised for target detection and offer covertness for the receive node [2], [94]. Unfortunately, there are not as many results for bistatic sea clutter when compared to the monostatic case. The few data well documented in the literature are reported in Table II (adapted from [22]). In this section, we will focus on results from the NetRAD radar system with the characterisation based on the geometry in Fig. 24 where ϕ_1 is the incidence angle, ϕ_2 is the scattering angle and the bistatic angle, $\beta = \arccos(\sin\phi_1 \sin\phi_2 - \cos\phi_1 \cos\phi_2 \cos\theta_{\text{B}})$. When the azimuth component of the bistatic angle, $\theta_{\text{B}} = 0°$ or $180°$,

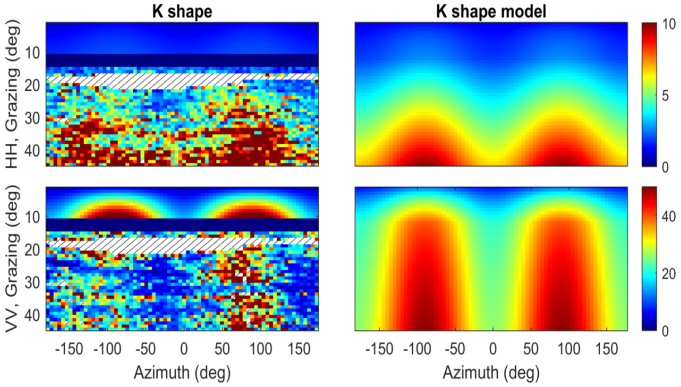

Fig. 23: K-distribution shape with resolution cell area $A_c = 756$ m^2. The data comprises the modified Watts and Wicks model for grazing angles $0.1° - 10°$ and the Ingara data from $15° - 45°$ [87].

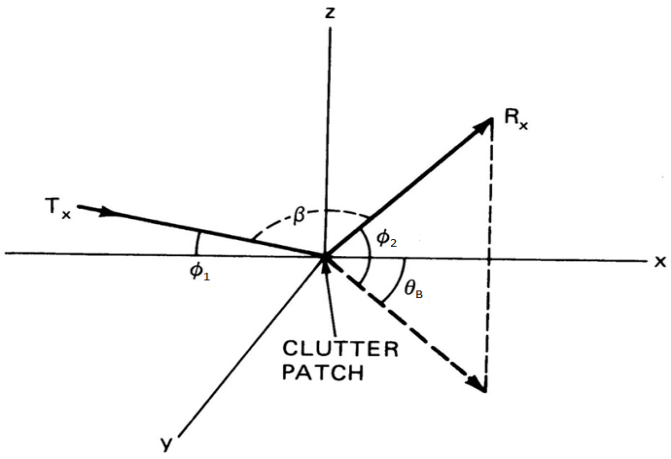

Fig. 24: Bistatic radar geometry, based on [96].

the scattering geometry is referred as in-plane, otherwise it is out-of-plane.

To determine the range cell area for the bistatic case, the footprint is determined by the intersection of the transmit and receive beams. Three cases are considered in [95], corresponding to the limiting cases of range, beamwidth and Doppler. Assuming small grazing angles and a large range sum compared to the baseline, $(r_T + r_R > L)$, then the range limited case has bistatic range resolution given by

$$\Delta r_b = \frac{c}{2B \cos\beta/2 \cos\varphi} \tag{33}$$

where φ is the angle from the bistatic bisector and a line connecting two potential targets. Assuming that the cross range of the receive beam is greater than that of the transmit beam, the bistatic range cell area is then given by

$$A_B = \frac{c r_T \theta_{3dB}}{2B \cos^2(\beta/2) \cos\varphi}. \tag{34}$$

TABLE II: Documented bistatic sea clutter experiments.

Organisation	Sea state	Freq.	Pol.	ϕ_1	ϕ_2	θ_B
John Hopkins University (1966-67)	1-3, 5	C-band X-band	VV, VH HH	0.2°-3° 1°-8°	10°-90° 12°-45°	180° 180°
GEC Stanmore (1967)	5	X-band	VV, HH	6°-90° ≈ 0°-90°	6°-180° ≈ 0°-180°	165°, 180°
Georgia Institute of Technology (1982-84)	3-4	X-band	VV, HH	≈ 0°	≈ 0°	90°-160°
NetRAD (UCL / UCT) (2010-2018)	3-4	S-band	VV, HH	≈ 1°	≈ 1°	60°-165°

A. Bistatic radar cross section

One of the main results on the mean backscatter of bistatic sea clutter has been presented by Domville in [97], after an extensive recording campaign with an X-band airborne continuous wave transmitter and a receiver in a second aircraft. This in-plane model has been summarised in [1] with an example shown in Fig. 25 for a windspeed of $U = 7.5$ m/s and the HH polarisation. In this figure, the two grazing angles are ϕ_1 and ϕ_2, where $\phi_1 = \phi_2$ corresponds to the monostatic case and $\phi_2 = 180 - \phi_1$ corresponds to specular scattering.

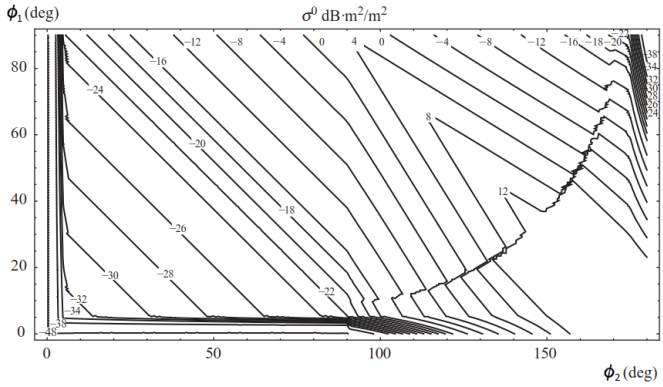

Fig. 25: Example of in-plane bistatic mean backscatter for the HH polarisation with a wind speed of 7.5 m/s [1].

Experimental results have been presented in [98] using data collected by the NetRAD system during a measurement campaign in 2010 at Scarbourough, Cape Town (see Section II-B). Table III reports the CNR and the mean backscatter in dBm^2/m^2 for the monostatic data, σ^0, and the bistatic data, σ^0_B. For almost all datasets, it was observed that the mean backscatter for the bistatic case is nearly always less than monostatic. Note that the monostatic results will vary with bistatic angle as the antenna's were pointing at a difference patch of the sea for each collection.

B. Amplitude distributions

A study of the bistatic sea clutter amplitude statistics has been reported in [98], [99] for the NetRad dataset on two different days with baselines of 1827 m and 728 m respectively. The statistical models used include the Weibull (W), K, Log-Normal (LN), Pareto (IG, in the following figures) and the Generalized Gaussian (|GG|). The shape and scale parameters of the theoretical distributions were estimated using the method of moments technique [100] and the data region contains only samples where the bistatic-clutter power

TABLE III: Summary of mean backscatter measurements for the NetRAD data (adapted from [98]). Note that the two VV $\beta = 90°$ measurements occurred at different times.

		Bistatic		Monostatic	
β	Pol.	CNR (dB)	σ^0_B (dB)	CNR (dB)	σ^0 (dB)
15°	VV	-7	-	-12	-
30°	VV	10.5	-59	8	-59
60°	VV	27	-47.9	26	-47.1
90°	VV	25	-55	33	-44.5
90°	VV	32	-47.8	39	-37.6
90°	HV	26	-55	16	-59.8
15°	HH	-10	-	-4	-
30°	HH	-15	-	-5	-
90°	HH	18	-61	31	-44.8

was high and the contribution from thermal noise was less significant.

For the datasets collected with the larger baseline, the LN and Pareto models have a good fit over the entire range extent, while the log-normal distribution is able to follow the tails of the data histograms where the clutter power is high. For the datasets with a small baseline, the data seems to be appropriately represented by the K distribution model, but the good fit of this model gets less precise when the clutter is less powerful. Two examples are shown in Fig. 26 for bistatic HH data with $\beta = 90°$, and bistatic VV data with $\beta = 60°$. Note that due to the geometry, the range cell under test, $r_{\text{CUT}} = 1380$ m for $\beta = 90°$ and $r_{\text{CUT}} = 1900$ m for $\beta = 60°$.

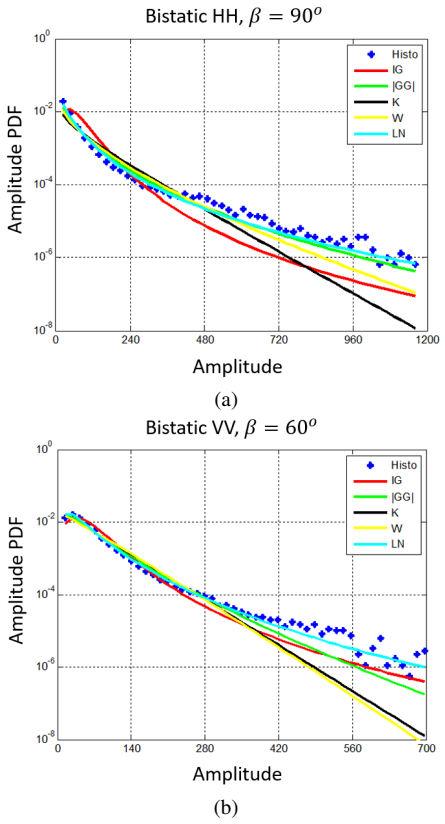

Fig. 26: NetRAD amplitude PDF for (a) bistatic HH data with $\beta = 90°$, (b) bistatic VV data with $\beta = 60°$ [99].

Further information about the spikiness of the data can be obtained by looking at the variation of Weibull shape parameter, c_{W} where small values indicate an increasing deviation from Gaussianity. The study in [99] found that for bistatic data, the HH shape parameter is almost always higher than for monostatic data. The behaviour is different in the VV polarisation, where the bistatic shape parameter is often smaller than the monostatic one. Based on these results, we can conclude that the bistatic clutter is less spiky than monostatic in the HH polarisation, while it is comparable for VV.

C. Texture correlation

The long time clutter correlation for the NetRAD bistatic data has been studied in [75] and is reproduced in Figs. 27 and 28 for the HH and VV polarisations. From these datasets it is apparent that for the monostatic HH data, the correlation time is only about 5 s, while for the HH bistatic data, the texture correlation exhibits a slightly periodic behaviour for $\beta = 90°$ and $\beta = 120°$ (not shown). In the VV data, this periodicity is much clearer for both monostatic and bistatic data, particularly for $\beta = 60°$ and $\beta = 90°$.

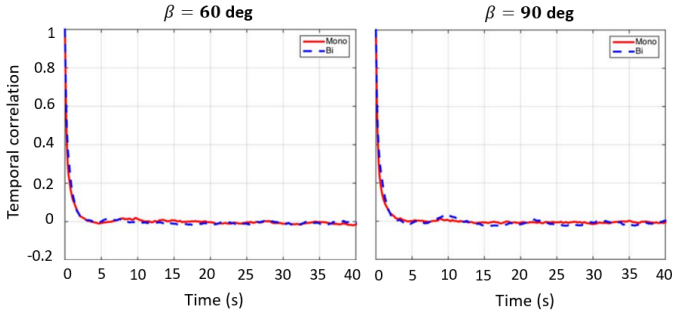

Fig. 27: Temporal correlation for the NetRAD HH data at $\beta = 60°$ and $\beta = 90°$ [75].

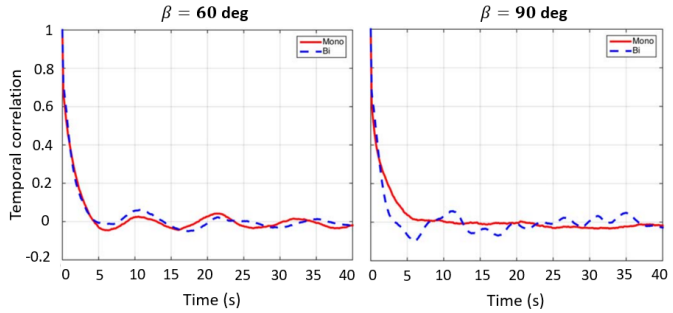

Fig. 28: Temporal correlation for the NetRAD VV data at $\beta = 60°$ and $\beta = 90°$ [75].

Another important aspect which influences the performance of multistatic detection schemes is the degree of texture cross correlation between the monostatic and bistatic nodes. This has been studied in [101] with the maximum values shown in Fig. 29 over a range of bistatic angles. In general, the maximum texture cross-correlation coefficient fluctuates between 0.2 and 0.5 for co-polarised data, and between 0.7 and 0.05 for cross-polarised data.

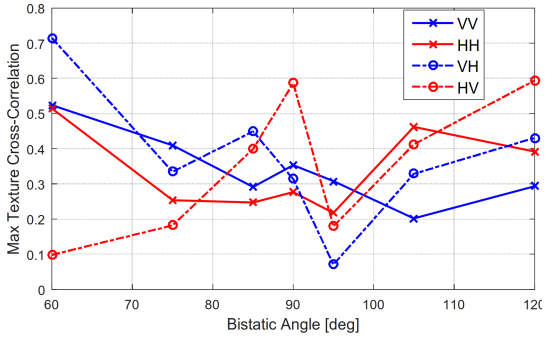

Fig. 29: Maximum texture cross correlation between the monostatic and bistatic nodes of the NetRAD data [101].

D. Sea spikes

To better understand the behaviour of the sea spike components, consider an example of the NetRAD time-history in Fig. 30 for a selected range cell of the bistatic and monostatic VV data. In this dataset, the bistatic angle is $\beta = 60°$ and the range cell under test $r_{\text{CUT}} = 1900$ m from the receivers. Although the monostatic data shows a power level higher than the bistatic data, the presence of spikes is evident in both plots. It can be noted that there is not a great correlation between the spiking events. For the bistatic data, one high spike with short duration is present at about 60 s, with other long spikes at 90 s and 115 s. On the other hand, the monostatic data shows only one spike at 80 s with other minor events at 45 s and 55 s.

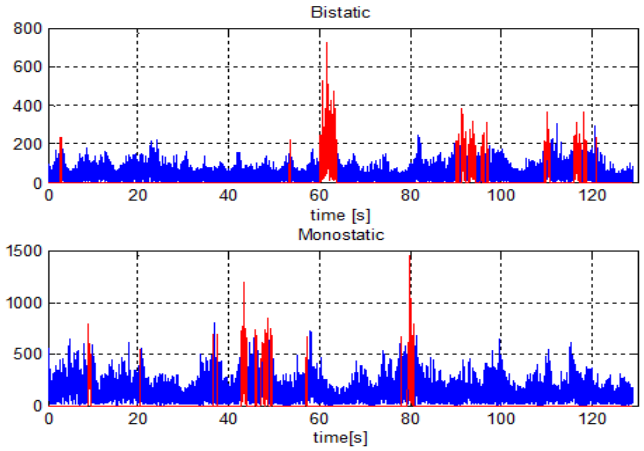

Fig. 30: Time history of the NetRAD amplitude clutter samples with VV polarisation and $\beta = 60°$. Selected spikes are plotted in red [99].

Fig. 31 shows the range-time map for $\beta = 60°$ [99]. In these results, the horizontal axis corresponds to the time in seconds and the vertical axis to a range interval where the bistatic CNR is high. The range-time diagrams are characterised by bands of high power, i.e. clusters of persistent spikes which migrate in range due to their velocity. The duration of this back-scattering contribution is similar to that of the whitecap component in Walker's model [59], since these persistent spikes last from one to about 20 s. The discrete sea spikes are contained within the high-power bands, meaning that they mainly occur on the crests of the sea waves. Together, the discrete and persistent spikes are generally considered as part of the same non-Bragg scattering component and are observed mostly in the HH polarised data, whereas the banded pattern shows a less uniform power level than in the VV polarised data. In general, discrete spikes occur mainly in horizontally polarised data both for the monostatic and bistatic data, but in the case of the vertical polarisation, the bistatic data seems to have a higher number of discrete spikes than the monostatic data [102].

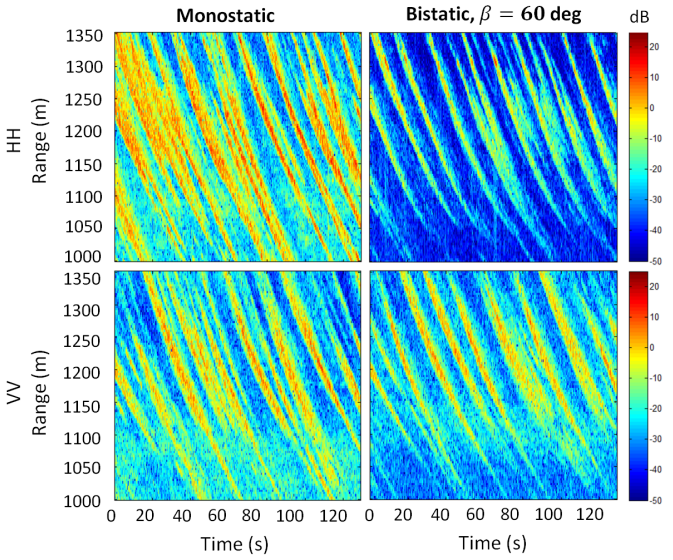

Fig. 31: Time domain image of the NetRAD bistatic data collected at $\beta = 60°$ [103].

Automatic classification of the sea spike components has been undertaken in [66] where spikes are defined as short echoes with an amplitude much higher than the background. Samples which have a power level higher than the power threshold and last longer than the minimum spike width are classified as spikes, and those spikes which have a separation smaller than the minimum interval are joined together to form one spike [66]. The power threshold was set as 6 times the mean power of the received returns, the minimum spike width was 80 ms and the minimum interval between spikes was 150 ms. These values were chosen empirically by evaluating the performance of the spike selection algorithm in the time-history plots of clutter samples and in the masks of selected spikes. Fig. 30 shows the time history of the amplitude clutter samples with the spikes highlighted in red, whereas Fig. 32 shows the mask of the selected sea spikes (same range interval as the range-time maps in Fig. 31), where a white pixel corresponds to a spiky sample. The figures confirm a good classification of the spiking events.

Once quantified, the statistics of the spike width in seconds and the time interval between spikes can be determined by forming histograms of the data and comparing them with an exponential PDF. Fig. 33 shows that the exponential distribution is a reasonable model for the spike width. The results in [66], [103] show that the mean spike width is higher for the

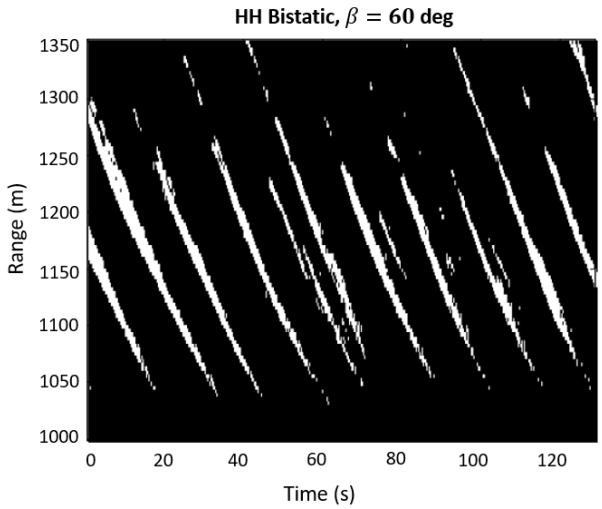

Fig. 32: Detection mask of the selected sea spikes for the NetRAD HH bistatic data collected at $\beta = 60°$ [103].

lower bistatic angles with longer spikes present in the bistatic VV data and most of the HH data. The mean interval between spikes is also generally higher for the bistatic data. Table IV summarises the results for $\beta = 60°$, showing the ratio of the number of samples belonging to a spike and the number of received samples, p_{sp}, the mean spike width, d_{m} and the mean interval between spikes, i_{m}.

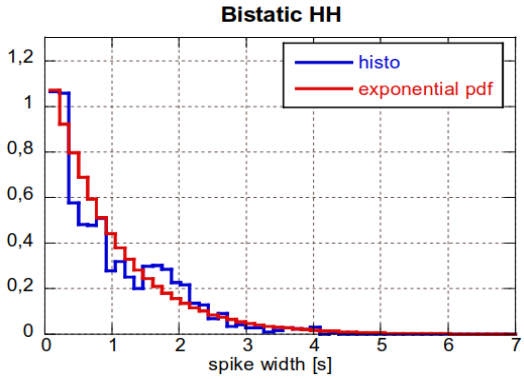

Fig. 33: Empirical distribution of spike width for the NetRAD bistatic HH data with $\beta = 60°$ [103].

TABLE IV: Average spike parameters in the NetRAD data for $\beta = 60°$ [103].

	Bi HH	Mono HH	Bi VV	Mono VV
p_{sp}	8.41%	13.25%	11.87%	12.17%
d_{m} (s)	0.93	0.75	1.22	1.00
i_{m} (s)	12.22	6.51	14.13	8.56

E. Doppler spectrum

In the open literature, there are few references focusing on the spectral characteristics of bistatic sea clutter. Some results for the NetRAD data have been illustrated in [75] using the unimodal Gaussian Doppler spectrum model in Section III-F.

To estimate the linear model for the mean in (27), the center of gravity (CoG) of the distribution must be measured as defined in [16]. Fig. 34 shows the CoG estimates plotted against the two-way range for HH data [75]. The results for $\beta = 90°$ and $120°$ show a trend of increasing CoG with range, while the bistatic data at $\beta = 60°$ shows a decrease in the CoG values with range. Similar behavior is evident in the monostatic data at $\beta = 60°$. The VV monostatic data (not shown) does not have the same increasing or decreasing behavior as in the HH case. Further results on the spectrum width can be found in [75]. Given the small amount of data, it is difficult to draw any strong conclusions on the spectral characteristics.

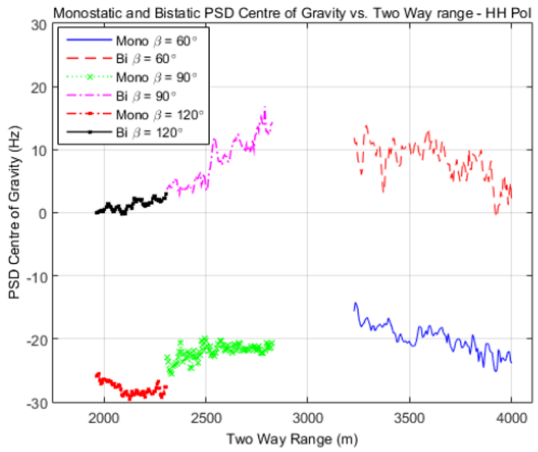

Fig. 34: Monostatic and bistatic centre of gravity for the NetRAD HH data [75].

F. Modelling bistatic sea clutter

Due to the complexities in measuring bistatic sea clutter, there are not many bistatic clutter models in the literature. The exception is the mean backscatter for both in-plane and out-of-plane geometries. Based on the work of Domville [97] and other experimental data, it has been observed that the bistatic mean backscatter is dominated by the return with the smallest grazing angle between the transmitter and receiver. Willis [104] has analysed the Domville data using Barton's model for bistatic land clutter [105], and proposed the following relationship,

$$\sigma^0_{\text{B}}(\phi_1, \phi_2) = \gamma \sqrt{\sin\phi_1 \sin\phi_2} \tag{35}$$

where γ is the constant gamma coefficient. To improve the accuracy of this model, Griffiths et al. [2] has proposed a variation using the monostatic GIT model, σ_{M}, calculated at both the transmit and receive nodes. If these values are used inside the geometric mean, the bistatic mean backscatter can be modelled as

$$\sigma^0_{\text{B}}(\phi_1, \phi_2, \theta) = \sqrt{\sigma_{\text{M}}(\phi_1, \theta)\sigma_{\text{M}}(\phi_2, \theta)}. \tag{36}$$

For out-of-plane bistatic mean backscatter, the change in azimuth angle requires two further effects to be modelled. These include a reduction of the co-polarised scattering component

and an increase in the cross-polarised component [2]. Both of these effects can be attributed to 'skew de-polarization', which is a projection of the electromagnetic field from the frame of the transmitting antenna to the frame of the receiving antenna. To model this effect, sinusoidal functions have been included in the model below with three variables, m, n and k adjusted to match the data. The model proposed in [2] uses Long's model [106] for the monostatic cross-polarised signal, $\sigma^0_{\mathrm{M_x}}$

$$\sigma^0_{\mathrm{M_x}}(\theta) = 10^{0.1(29.8\ln(0.5144U)+6\cos\theta-84.7)}. \tag{37}$$

Then assuming that the co-polar and cross-polar components add incoherently, the complete model is given by

$$\sigma^0_{\mathrm{B}}(\phi_1,\phi_2,\theta_{\mathrm{B}}) = \sqrt{\sigma^0_{\mathrm{M}}(\phi_1,0)\sigma^0_{\mathrm{M}}(\phi_2,\theta_{\mathrm{B}})|}\cos\theta_{\mathrm{B}}|^m + k\sqrt{\sigma^0_{\mathrm{M_x}}(0)\sigma^0_{\mathrm{M_x}}(\theta_{\mathrm{B}})|}\sin\theta_{\mathrm{B}}|^n, \quad k,m,n>0. \tag{38}$$

V. Simulation of Radar Sea Clutter

One of the ways that models of sea clutter are used is to simulate realistic clutter signals. These can be used to stimulate radar processors during development and testing, generate realistic responses and displays in radar trainers and to evaluate radar detection algorithms. A simulated signal must reproduce as faithfully as possible the characteristics of real clutter including its amplitude statistics, short-term temporal correlation (including that represented by the Doppler spectra) and spatial and longer-term temporal variations. It must also represent the variation of range and azimuth over time as observed from a wide-area surveillance radar. Finally to simulate realistic clutter from an airborne radar, it is important to model the effects of aircraft motion on the radar returns.

Many of the techniques discussed here are presented in [1]. We shall restrict discussions to the simulation of sea clutter represented by compound Gaussian models and, in particular, the K and Pareto distributions. As discussed in Section III-B, compound models have a Gaussian speckle component, a texture component and temporal and spatial correlations. The texture is approximately constant within a cell-under-test (CUT) over the tens of milliseconds typically associated with a radar dwell. This value will have a PDF given by a gamma distribution (K model) or an inverse-gamma distribution (Pareto model), and contain both spatial and long-term temporal correlations. The intensity of the speckle component will have an exponential PDF, modulated in power by the local texture. When using pulse to pulse frequency agility, this fluctuation will be approximately random and for a fixed frequency radar will fluctuate according to a short-term temporal correlation, usually modelled by a Doppler spectrum. It may be noted that although it is convenient to model clutter behaviour using autocorrelation functions and spectra, most clutter returns are time-varying and range-varying and cannot be represented by a stationary stochastic process with complete accuracy.

In order to simulate sea clutter returns, it is convenient to generate the texture and speckle components separately. The sections below first show how the memoryless nonlinear transform (MNLT) may be used to generate texture samples. This is followed by methods for generating coherent and non-coherent speckle signals.

A. Clutter texture simulation with the memoryless non-linear transform

The MNLT is a fairly straightforward way to transform a set of random Gaussian-distributed variables to have a different PDF. Samples are first generated from a zero mean, unit variance Gaussian process and for each sample value p, the cumulative distribution of the Gaussian process at that point is equated to a cumulative distribution with the desired PDF, P_{dist} evaluated at q. For successive random samples, the resulting values q will then have the required PDF. This can be written as

$$\int_q^\infty P_{\mathrm{dist}}(q')dq' = \frac{1}{\sqrt{2\pi}}\int_p^\infty \exp\left(-\frac{p'^2}{2}\right)dp' = \frac{1}{2}\mathrm{erfc}\left(\frac{p}{\sqrt{2}}\right). \tag{39}$$

where $\mathrm{erfc}(\cdot)$ is the complementary error function. If we then define the complementary quantile function, Q, so that

$$\int_{Q(\kappa)}^\infty P_{\mathrm{dist}}(q)dq = \kappa, \tag{40}$$

the required value q can be given by

$$q(p) = Q\left(\frac{1}{2}\mathrm{erfc}\left(\frac{p}{\sqrt{2}}\right)\right). \tag{41}$$

For example, if we want to generate a gamma distribution with

$$P_{\mathrm{dist}}(p) = \frac{1}{\Gamma(\nu)}p^{\nu-1}e^{-p}, \tag{42}$$

then

$$\int_{Q(\kappa)}^\infty P_{\mathrm{dist}}(q)dq = \frac{\Gamma(\nu,Q(\kappa))}{\Gamma(\nu)} = \frac{1}{2}\mathrm{erfc}\left(\frac{p}{\sqrt{2}}\right). \tag{43}$$

and the gamma random variable is recovered by solving this relationship and evaluating the quantile function. Quantile functions of various functions are available in packages such as Mathematica [107].

B. Clutter texture simulation with correlated samples

It is easy to generate Gaussian samples with a desired spectrum or autocorrelation function (ACF) using filtering techniques in the time or frequency domains. For example, if the required correlation coefficient is $\rho(t)$ for slow-time t, then the equivalent power spectral density $S(f)$ can be determined by the Fourier transform, $\mathcal{F}[\rho(t)]$. To generate a sequence of M samples, a voltage spectrum is generated as $\sqrt{\mathcal{F}[\rho(t)]}$, multiplied by a vector of M random Gaussian samples with zero mean and variance 1, $\mathcal{N}[0,1]$, and then transformed back to the time domain. The mean level and standard deviation of the real component of the transformed data are then adjusted to give the required values. A 2-dimensional array of correlated samples can be generated in a similar way.

However, if correlated Gaussian samples are transformed using the MNLT, the resulting samples will have the desired

PDF but their ACF will have changed. Within some limitations discussed below it is possible to determine the ACF that the Gaussian samples should have to achieve the required ACF.

The relationship between the ACFs at the input and output of the MNLT was first described in [108]. As illustrated below and examined in [109], there are some limitations to the mappings that can achieved. A good illustration of the method with specific application to the simulation of K distributed sea clutter is presented in [110], with further details in [1]. If the ACF of the transformed variables, y, is given by $\langle y(0)y(t)\rangle$ it can be shown that the desired normalised ACF $R_G(t)$ of the Gaussian samples is related by

$$\langle y(0)y(t)\rangle = \frac{1}{2\pi}\sum_{n=0}^{\infty}\frac{R_{\rm G}(t)^n}{2^n n!} \times \left(\int_{-\infty}^{\infty} e^{-x^2/2} H\left(\frac{x}{\sqrt{2}}\right) Q\left(0.5\text{erfc}\left(\frac{x}{\sqrt{2}}\right)\right) dx\right)^2 \quad (44)$$

where $H(x)$ is a Hermite polynomial, readily accessible in packages like Mathematica [107]. This expression looks complicated but can readily be processed using numerical computing methods. Usually, only a few terms of the infinite summations are required. This method has the advantage that it can reproduce samples with negative values of correlation coefficient.

As an example, we can illustrate the generation of gamma distributed samples. If we set $\langle y\rangle = 1$, then $\langle y^2\rangle = 1 + 1/\nu$ and if the required correlation coefficient is $\rho(t)$, then $\langle y(0)y(t)\rangle = 1 + \rho(t)/\nu$. Now (44) can be solved to give

$$\langle y(0)y(t)\rangle = f(0) + f(1)R_{\rm G}(t) + f(2)R_{\rm G}^2(t) + \ldots \quad (45)$$

This result has to be inverted for each value of the lag, t, to find the required values of $R_{\rm G}(t)$. It is then a simple matter to generate Gaussian samples with the required ACF, as discussed above. Fig. 35 shows examples of the mapping between the desired correlation coefficient of gamma distributed variables, $\rho(t)$, and the correlation coefficient of the Gaussian variables $R_{\rm G}(t)$, prior to application of the MNLT. For $\nu = \infty$, the mapping is $1:1$ but as ν reduces it is not possible to map all negative values of $\rho(t)$ onto $R_{\rm G}(t)$. For example with $\nu = 0.1$, only $\rho(t) > -0.1$ can be modelled.

The method can also be applied in two dimensions to simulate an area of sea. An example is shown in Fig. 36 with the correlation coefficient modelled as

$$\rho(m_1, m_2) = \exp\left(-\frac{|m_1| + |m_2|}{10}\right)\cos\left(\frac{\pi|m_2|}{8}\right) \quad (46)$$

with $-\infty \le m_1, m_2 \le \infty$ and the gamma shape parameter, $\nu = 2$.

As discussed above, there are some limitations to the values of negative correlation coefficient that can be achieved by this method, especially in very spiky clutter. Some other methods of producing correlated gamma variates are described in [111], [112]. However, these methods lack the ability to introduce anti-correlations or are only approximate solutions that do not reproduce the higher order moments correctly. The use of an MNLT is proposed in [113], but does not address the general solution for an arbitrary ACF. Despite the limitations of the method proposed here, it is found in practice that it is usually possible to adequately reproduce the ACFs and PDFs encountered in real sea clutter. It should also be remembered that this is only a model of sea clutter. This representation may not fully represent the large discrete sea spikes sometimes observed, which may have a significant effect on radar performance. In these circumstances it may be necessary to treat clutter spikes separately.

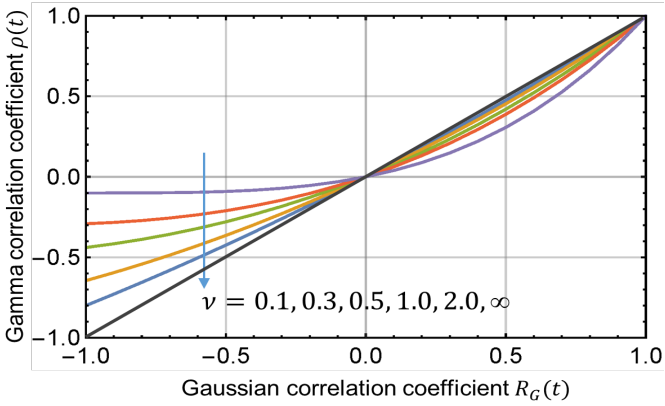

Fig. 35: Mapping between the correlation coefficient of gamma distributed variables, $\rho(t)$, and the correlation coefficient of the Gaussian variables $R_{\rm G}(t)$, for various values of gamma shape parameter, ν.

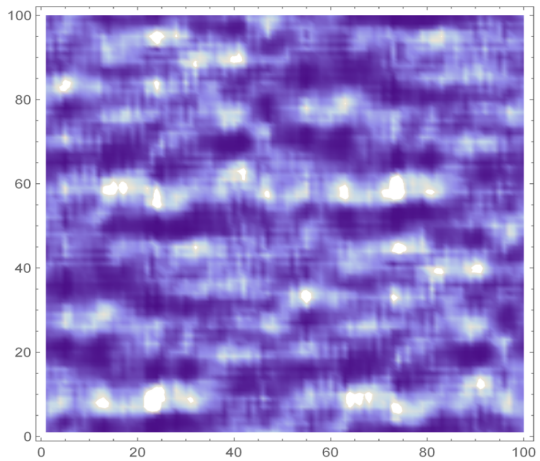

Fig. 36: A gamma distributed random field with $\nu = 2$ and correlation coefficient given by (46).

C. Non-coherent amplitude or intensity speckle samples

Once samples of the texture component have been generated they can be used to modulate the power of the speckle component. For a coherent signal, the speckle will be represented by a complex Gaussian process, which may also be correlated. The envelope of the returns will have a Rayleigh distribution and the intensity or power of the returns will have an exponential distribution. For many applications, the non-coherent speckle signals are assumed to be either fully correlated or independent from pulse to pulse. In that case

suitable samples with Rayleigh or exponential distributions are easily generated using standard methods. Alternatively, a more precise result can be obtained by generating sequences of complex Gaussian samples with an appropriate Doppler spectrum and then forming with modulus or modulus squared as appropriate.

D. Coherent speckle samples

As discussed in Section III-F, the spectrum of the speckle component can be modelled as having a Gaussian-shaped spectrum, with a randomly fluctuating spectrum width and a mean Doppler shift that may vary with the local intensity (dependent on the wind direction). This model was originally proposed in [72], [114] and its use for simulating data has been further developed in [76]. The model parameters have also been measured over a wide range of sea conditions and viewing geometries at X-band [27], [72], [77], [92], [115]), which is an important pre-requisite for the use of models in radar design.

1) Simulation in the frequency domain: To generate clutter samples directly in the frequency domain, the average power spectrum for the n^{th} frequency bin at a given range and burst is defined as:

$$G(n,x) = \frac{x}{\sqrt{2\pi s}} \exp\left(- \frac{\left(\left(n - \frac{N}{2}\right) \frac{f_r}{N} - m_f(x) \right)^2}{2s^2} \right) \quad (47)$$

where $n = 1, \ldots, N$ and the local intensity of the texture is x. The spectrum is defined here to have 0 Hz centred on frequency bin $N/2$. The parameters of simulation defined previously include the PRF, f_r, the number of pulses in a burst, N, the spectrum mean Doppler parameters A, B, the spectrum width parameters m_s, σ_s, the shape parameter of the clutter, ν and the CNR, C. The coherent spectra are then generated as

$$S(n,x) = \sqrt{G(n,x)} g(n) + \gamma(n) \quad (48)$$

where $g(n)$ are random complex samples with a Gaussian PDF of the form $\mathcal{N}[0,1] + j\mathcal{N}[0,1]$ and $\gamma(n)$ are complex noise samples. If $\left\langle \sum_{n=1}^{N_b} G(n,x) \right\rangle = 1$, then $\gamma(n)$ will have the form

$$\gamma(n) = \mathcal{N}[0, \sqrt{N/(2C)}] + j\mathcal{N}[0, \sqrt{N/(2C)}]. \quad (49)$$

Finally, complex time domain samples for each burst can obtained by an inverse Fourier transform,

$$s(n,x) = \mathcal{F}^{-1}\left[\sqrt{G(n,x)} g(n) + \gamma(n) \right]. \quad (50)$$

2) Simulation in the time domain: If it is desirable to simulate longer returns from range gates which evolve in time and do not have discontinuities from concatenating data blocks with different values of mean intensity, then coherent time domain data with a continuously changing spectrum can be simulated [72]. For given values of x and s, a finite impulse response (FIR) filter can be designed and applied to coherent samples taken from a zero-mean complex Normal distribution. Over time in a given range gate, x and s will slowly change and if new values are defined for each PRI, the FIR filter weight can be changed from pulse to pulse. Provided that x and s only change very slowly (at least with respect to the length of a few pulse bursts), the resulting data should have a defined spectrum with the required characteristics. Consider an FIR filter of length L having weights of the form:

$$w(l, x_{m_1,m_2}, s_{m_1,m_2}) = \sqrt{\frac{x_{m_1,m_2}}{2}} \exp\left(-jm_f(x_{m_1,m_2}) \frac{2\pi l}{f_r} \right) \times \exp\left(- \left(\frac{2\pi s_{m_1,m_2} l}{f_r} \right)^2 \right) \quad (51)$$

for $l = -L/2, \ldots, 0, \ldots, L/2$, where the sampling interval is $1/f_r$. Now x_{m_1,m_2} and s_{m_1,m_2} are the values of x and s defined for range m_1 and azimuth m_2, as in (46). If the filter weights change slowly enough for each pulse, the resulting data will then have an appropriate time-varying spectrum. For best fidelity, it may be appropriate to either increase the PRF and later down-sample as required, or increase the length of the filter, L. A possible guideline is that $sL/f_r \approx 1$.

3) Summary of coherent sea clutter simulation: The steps required to generate complex bursts of data at different range gates include:

1) Define the correlation coefficient $\rho(\cdot)$ of the intensity, x, as a function of range and, in general, from pulse to pulse. For the generation of successive bursts of data at a given range, the intensity is assumed to be constant over a burst, so the correlation coefficient can be defined from burst to burst. For the direct generation of time-series data described in Section V-D2, the correlation from pulse to pulse will be required.
2) Define the equivalent correlation coefficient for the spectrum standard deviation, s.
3) Generate a 2-dimensional array of correlated samples, x, with a gamma or inverse gamma distribution having shape parameter ν and unit mean level (assuming the K or Pareto distribution models are being used).
4) Generate a 2-dimensional array of correlated samples, s, with a gamma or Gaussian distribution and mean m_s, and standard deviation, σ_s.
5) Define other simulation parameters.
6) Generate complex spectra as described above and transform to the time domain if required/appropriate.

As an example, Fig. 37 shows a simulated series of power spectrum from one range gate over a period of 32 s, while Fig. 38 shows a reasonable match of the original and simulated texture correlation. The modelled parameters are taken from real data with $\nu = 0.4$, $m_s = 59$ Hz, $\sigma_s = 4.7$ Hz, $A = 5$ Hz, $B = 5$ Hz, $f_r = 5$ kHz and $M = 64$ pulses.

E. Platform motion and antenna scanning

The effects of platform motion and antenna scanning can also be incorporated in the coherent clutter simulation. The simplest approach is to assume a Gaussian-shaped spatially homogenous spectrum, as defined in (47), with the standard

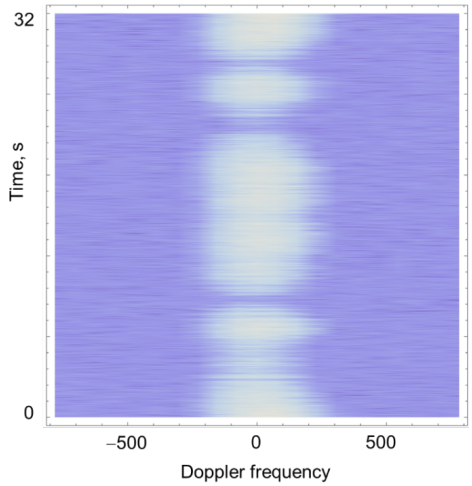

Fig. 37: Simulated power spectra.

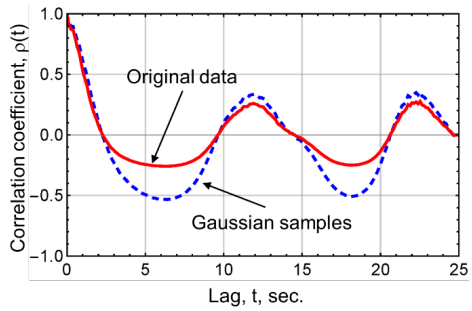

Fig. 38: Correlation coefficient of the texture component and the Gaussian samples before MNLT.

deviation of the spectrum increased to $\sqrt{s^2 + s_{\text{plat}}^2}$ with

$$s_{\text{plat}} \approx \frac{0.6\theta_{3\text{dB}} v_{\text{p}} |\sin\psi_0|}{\lambda}, \tag{52}$$

where v_{p} is the platform velocity and ψ_0 is the antenna look direction relative to the platform track ($\psi_0 = 0$ is along-track).

A point target or discrete clutter spike within the beam will also have its spectrum broadened due to azimuth scanning of the antenna, even from a stationary platform. For a dwell that matches the full beamwidth of the antenna, the spectrum will be broadened by an additional component s_{scan}, where

$$s_{\text{scan}} = \frac{0.265\dot{\theta}_{\text{scan}}}{\theta_{3\text{dB}}} \tag{53}$$

and $\dot{\theta}_{\text{scan}}$ is the antenna azimuth scanning rate. In the bimodal version of the clutter model (see Section III-F) the broadening might be applicable to the second higher Doppler frequency component. If the processing dwell is significantly less than an antenna beamwidth, this effect may be ignored.

F. Multiple antenna apertures

Modelling the sea clutter return from multiple antennas in an array is often desired in order to investigate techniques such as space time adaptive processing, adaptive beamforming, along-track interferometry and similar techniques. Ideally, this requires a knowledge of the spatial disposition of scatterers within the radar beam, but this is beyond the capability of current models. However, some headway can be made by considering a spatially distributed model of the clutter being uniformly spread across the radar beam. The techniques presented here were originally published in [78], and later extended to a scanning radar in [79]. Another technique for simulating the coherent return from multiple phase centres has recently been published by McDonald and Cerutti-Maori in [32].

1) Model construction: When modelling the simultaneous returns from multiple phase centres, it will be necessary to sub-divide the clutter patch into N_{s} sub-patches, where the centre of each patch subtends an angle θ_k from the centre of the array and $k = 1, \ldots, N_s$. In general $N_{\text{s}} \gg 1$ within the antenna main beam and it is important that the sub-patches also extend over the antenna sidelobes if a moving platform is to be modelled. Fig. 39 shows two antenna phase centres separated by D, and at a distance R_0 from the clutter patch.

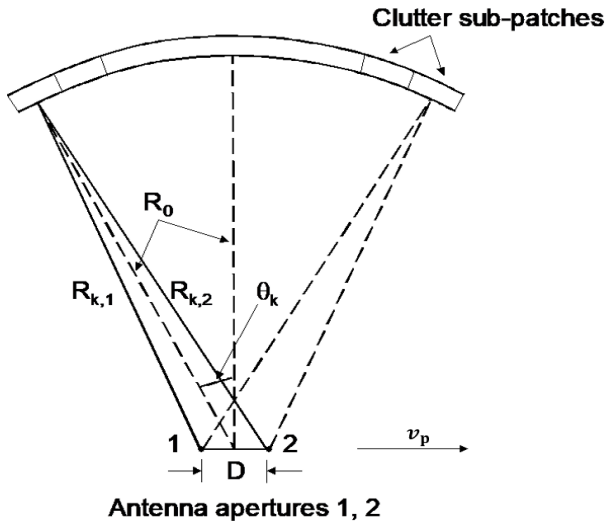

Fig. 39: Geometry of clutter sub-patches observed by two phase-centres [78].

For a single aperture, the returns from the sub-patches should combine to give a mean value equal to the local clutter texture, x. When considering two or more apertures, the relative phase of the returns from the sub-patches at each antenna aperture must be modelled. At a given range, R_0, the total intensity of the returns from all clutter sub-patches are weighted by the one way antenna beam pattern, $F(\theta_k)$ and are equal to the local mean intensity,

$$\sum_{k=1}^{N_s} x_k = x \tag{54}$$

where the mean power for the k^{th} patch is $x_k = F(\theta_k)x$. The sub-patches do not need to be the same size or uniformly spaced across the aperture.

We will assume that returns from each sub-patch in the time domain are given by $s(t_n, x_k)$, where the time is sampled at the pulse repetition interval, T, over a coherent processing

interval of N samples with $t_n = nT$. We will also make the initial assumption that the returns from each sub-patch have the same normalised power spectral density, but are independent of each other (i.e. with an independent speckle component). The average power spectrum at a given range and sub-patch is then defined as $G(n, x_k)$ using the definition in (47). Note that the values of x and s are the same for each average spectrum with only x_k changing. The coherent spectra are then generated as

$$S(n, x_k) = \sqrt{G(n, x_k)}g(n) \tag{55}$$

and complex time domain samples for each sub-patch are given by $s(t_n, x_k) = \mathcal{F}[S(n, x_k)]$ with the total return in a single aperture given by

$$s(t_n, x) = \sum_{k=1}^{N_s} s(t_n, x_k). \tag{56}$$

At this point, discrete spikes can also be added to the returns if required. These may be modelled as a point response at a particular position within the beam, or as a distributed return arising across two or more clutter sub-patches. Each spike can be given its own power spectral density.

When observed simultaneously by two apertures, the geometry over the main beam in the far field is shown in Fig. 39. Assuming that the transmitter phase centre is located at the centre of the array, the phase difference φ_k between returns in the two apertures is

$$\varphi_k = \frac{2\pi}{\lambda}\left(R_{k,2} - R_{k,1}\right) \approx \frac{2\pi D \sin\theta_k}{\lambda} \tag{57}$$

where $R_{k,1}$ and $R_{k,2}$ are the ranges from phase centres 1 and 2 respectively to the k^{th} clutter sub-patch. It is assumed for simplicity that the antenna beam is pointing normal to the array but in general any squint angle can be modelled. Also, if the antennas are moving with an along-track velocity v_p, then the phase from each clutter sub-patch will increment or decrement from pulse to pulse due to the change in platform position. So now for two phase centres,

$$\begin{aligned} s_1(t_n, x) &= \sum_{k=1}^{N_s} s(t_n, x_k) \exp\left(j\frac{2\pi v_\mathrm{p} t_n}{\lambda}\sin\theta_k\right), \\ s_2(t_n, x) &= \sum_{k=1}^{N_s} s(t_n, x_k) \exp\left(j\varphi_k\right) \exp\left(j\frac{2\pi v_\mathrm{p} t_n}{\lambda}\sin\theta_k\right). \end{aligned} \tag{58}$$

where the power spectral densities will be the same for the returns in each aperture, but their phase relationships will be a function of the aperture spacing. Finally, thermal noise can be added as complex Gaussian samples to the time domain returns in each channel, according to the CNR required.

Apart from any discrete spikes that may be added, this model assumes that the normalised power spectral density of the clutter returns is the same in each clutter sub-patch. However, this is just for convenience and each clutter sub-patch could have a different normalised power spectral density. For example, the clutter returns observed through the antenna sidelobes may have a power spectral density that varies with look direction. Also, the areas of the sub-patches or their angular spacing does not need to be equal. In fact, an uneven spacing may help to avoid artefacts in any angle-dependent processing of the returns.

2) Summary for simulation of two or more phase-centres: The following steps should be followed to simulate correlated returns from multiple phase-centres. The method can easily be extended to multiple phase-centres.

1) If simulating returns in successive range gates, generate an array of correlated values of x, having a Gamma distribution, with shape parameter ν.
2) Determine the power spectral density of the returns at each range, according to the spectrum model being used.
3) For each range gate, divide the antenna beam into N_s angular sectors, giving N_s clutter sub-patches. The accuracy should improve as N_s increases.
4) Calculate the mean intensity of the return in each clutter sub-patch according to (54).
5) For each clutter sub-patch, generate a complex spectrum with the appropriate weighted mean intensity and random values of speckle as shown in (55).
6) Transform each complex spectrum into the time domain, giving N values of a complex time domain series $s(t_n, x_k)$ for each sub-patch.
7) Add discrete spikes as required.
8) Apply the appropriate phase weighting to the returns from each sub-patch and sum over all sub-patches to give $s_1(t_n, x)$ and $s_2(t_n, x)$, as shown in (58).
9) Add thermal noise independently to each channel.

VI. Radar performance prediction in sea clutter

One of the important uses of models of sea clutter is in the prediction of radar performance. This is an essential part of the design, development, assessment and marketing of radar systems. The essential methods for predicting the performance of radars in sea clutter are described in detail in [1]. The radar range equation in (3) is used to estimate the power received from targets, clutter and thermal noise. This requires knowledge of the radar parameters, the losses within the radar, the atmospheric losses, propagation effects, the prevailing weather conditions, the viewing geometry and so on. Many of these terms require a significant amount of effort to define accurately. For example, losses in the radar will include microwave losses in the radar, antenna and radome, together with filter mismatch losses within the receiver. Propagation effects will include attenuation due to the atmosphere, clouds and precipitation (which will vary with frequency and altitude) and may also include ducting, which affects detection ranges and apparent local grazing angles. It may also be necessary to undertake a very detailed analysis of the radar signal processing to fully assess the effects of receiver frequency response, mismatch losses, sampling losses, quantisation losses, etc. Often these are not strictly losses, but represent actual performance compared with idealised assumptions made when analysing performance (i.e. constant false alarm rate (CFAR) losses, integration losses, etc.).

When assessing the detection performance, the clutter, target and noise power levels are first estimated. These power levels

are usually defined at a point in the receiver where the noise bandwidth and noise figure are fully defined, but prior to any signal processing or detection/demodulation stages. For sea clutter returns, the appropriate level of σ^0 is obtained from a chosen model as discussed in Section III-G.

The effect of any coherent signal processing prior to the first threshold stage must then be assessed. Coherent processing over a dwell will require models of the target and clutter Doppler spectra, as discussed below. The aim is to achieve estimates of the target, clutter and noise levels following such processing (e.g. in each Doppler bin following a Doppler filtering operation) prior to a detection threshold.

For non-coherent processing following a non-linear processing stage, the assessment is potentially more complex as the statistics of the combined target, clutter and noise signals will be different. These statistics will be further modified by pulse-to-pulse integration. This is discussed in detail in [1] for detection in K distributed sea clutter, with a similar analysis in [47], [116] for detection in K and Pareto-distributed clutter.

Following detection there may be further data processing stages such as range collapsing, scan-to-scan-integration and tracking. The effect of these on the final probabilities of detection and false alarm must also be calculated. Given the desired performance at the radar output (i.e. the radar display, tracker performance, etc.), it is then possible to work backwards to the required performance at the first detection threshold where analytic calculations are usually made. Scan-to-scan integration may be particularly important when sea clutter spikes are detected. These may have durations of a second or more and appear target-like with a single beam dwell of a scanning radar. However, by integrating from scan-to-scan over several seconds, the spikes may be suppressed in relation to a more persistent target.

A. Detection in compound Gaussian clutter

The compound Gaussian models of sea clutter was given in (12) with the speckle PDF given by $P(Z|x)$ and the texture PDF by $P(x)$. The probability of false alarm, P_{fa} is equivalent to the CCDF and is defined with a threshold τ,

$$P_{\text{fa}}(\tau) = \int_{\tau}^{\infty} \int_{0}^{\infty} P(Z|x)P(x)dxdZ \tag{59}$$

$$= \int_{0}^{\infty} \frac{\Gamma\left(M, \tau/(x+p_{\text{n}})\right)}{\Gamma(M)} P(x)dx \tag{60}$$

and must be evaluated numerically. If the clutter speckle component is not independent from pulse to pulse (for example, if the radar is operating with a fixed frequency), the calculations are more difficult and the reader is referred to [1], [47], [116].

To assess the probability of detection, the target PDF must be appropriately modelled. The Swerling target models are often used [117] and a generalised gamma model can be used to extend the range of fluctuation characteristics [118]. The simplest case is the Swerling Case 2 target model which has a noise-like RCS (an exponential PDF of intensity), fluctuating randomly from pulse to pulse. This type of fluctuation may be encountered with extended range targets (at least filling a resolution cell) which are rapidly rotating or observed with a frequency-agile waveform. The single look PDF for a Swerling Case 2 target with added clutter speckle and noise is given by

$$P(z|x) = \frac{1}{x + p_{\text{n}} + p_{\text{s}}} \exp\left[-\frac{z}{x + p_{\text{n}} + p_{\text{s}}}\right]. \tag{61}$$

Pulse-to-pulse integration and averaging over all values of x can be undertaken as for clutter and noise alone. For a discussion on analysis techniques for more complex targets, see [1], [47].

B. Coherent detection prediction

The assessment of coherent processing requires a knowledge of the spectrum of the target and clutter in the CUT, as well as their amplitude statistics. There are many different detection schemes that have been proposed for use with targets in compound Gaussian clutter [119]. Simple Doppler filtering with an independently controlled threshold in each Doppler bin has been used in many radars. This makes no assumptions about the spectrum characteristics, but is not necessarily the best approach as controlling false alarms at the edges of the spectrum can be difficult [120]. If the clutter has compound Gaussian statistics, the optimum approach is to whiten the clutter-plus-noise in the CUT [119], [121]. However, this requires knowledge of the covariance matrix of the clutter-plus-noise, which is in general unknown. Many schemes have been proposed for estimating the covariance matrix from surrounding range cells [122]–[127]. However, the assessment of their performance is usually predicated on the clutter being a spherically invariant random process. This assumes that the texture and speckle are mutually independent processes and that the normalised covariance matrix of the speckle can be estimated by averaging over surrounding cells. However, the observations of real clutter, that lead to the model described in Section III-F, suggest that the mean Doppler shift may in fact often be correlated with the local texture and the normalised covariance matrix fluctuates randomly from one cell to the next. The ability to estimate a covariance matrix from surrounding cells is then dependent on the spatial correlation of the spectrum characteristics.

A recent review of the performance of different detection schemes in real sea clutter is given in [128]. It is not the intention here to explore all the different coherent detection techniques that have been proposed, but to indicate how clutter models can be used to assess their performance. The models of Doppler spectra, as described in Section III-F can be used in the prediction of performance. If simple Doppler filtering is considered, the clutter, noise and target levels must be predicted at the output of the filters. In addition, depending on how the detection threshold is set, the amplitude statistics of the signals in each Doppler bin must be estimated with consideration for how they vary over range or time.

1) Doppler filtering: The effect of the range-varying spectrum width and mean is to change the statistics of the clutter intensity in each Doppler bin. This is most significant near the edges of the spectra where the clutter statistics become spikier (see for example, [1, Chapter 2]). Using the spectrum model in Section III-F, this effect can be estimated using the moments

of the clutter intensity in each Doppler bin, $x'(f_d)$, averaged over all possible values of x and s. Assuming Doppler analysis of an idealised filter with N pulses, pass-band $\Delta f = f_\mathrm{r}/N$:

$$\langle x'(f_d)\rangle = \int_{f_d-\frac{\Delta_f}{2}}^{f_d-\frac{\Delta_f}{2}} \int_0^\infty \int_0^\infty P(s)P(x)G(f,x,s)dxdsdf,$$
$$\langle x'(f_d)^2\rangle = \int_{f_d-\frac{\Delta_f}{2}}^{f_d-\frac{\Delta_f}{2}} \int_0^\infty \int_0^\infty P(s)P(x)G^2(f,x,s)dxdsdf \tag{62}$$

where $P(s)$ is the PDF of the spectrum width. If the noise power in each Doppler bin is related to the overall CNR by

$$p_\mathrm{n} = \frac{\langle x\rangle}{C.N}, \tag{63}$$

then the CNR in each Doppler bin, $C'(f_d)$, for the idealised Doppler filter will be

$$C'(f_d) = \frac{\langle x'(f_d)\rangle}{p_\mathrm{n}}. \tag{64}$$

It has been found that the amplitude statistics in individual Doppler bins can be modelled with a K plus noise distribution [74]. This suggests that the moments of intensity for each Doppler bin, given in (62) could be fitted to a gamma distribution, to determine the shape parameter $\nu'(f_d)$ in each Doppler bin so that

$$\nu'(f_d) = \left(\frac{\langle x'(f_d)^2\rangle}{\langle x'(f_d)\rangle^2 - 1}\right)^{-1}. \tag{65}$$

Using this method, the power levels and amplitude statistics of the clutter and noise can be predicted in each Doppler bin. The methods from Section VI-A can then be used to predict detection performance.

2) Whitening filters: The performance impact of pre-Doppler or post-Doppler whitening filters can also be studied using these models, [120], [128]. For example, in [129], the effects of errors in the estimation of spectra or covariance matrices was analysed. A more direct approach is to use Monte Carlo methods with simulated data to assess performance [120], [128]. This has the advantage of incorporating the effects of range-varying and time-varying spectra on estimates of the covariance matrices, but requires large data samples to accurately assess the performance for each set of conditions.

C. Performance prediction using simulated data

As discussed above, some aspects of detection in sea clutter are difficult to analyse and it may be necessary to resort to simulation and Monte Carlo methods. For non-coherent processing, a good example is the cell-averaging CFAR detector, which predicts the mean level of the CUT from the surrounding range cells. The statistical nature of such an estimate leads to a CFAR loss when compared to an exact knowledge of the mean level in the CUT. If the clutter is highly spatially correlated, for example in the presence of a long sea swell pattern, a better estimate of the local value of intensity can be obtained using a shorter cell-average length instead of the overall mean level. This may even lead to a potential 'CFAR gain' as opposed to the usual loss (see for example [1, Chapter 13]). Such performance can only be predicted and quantified with simulation methods.

As discussed above, some coherent detectors attempt to estimate the covariance matrix of the CUT from surrounding range cells. To fully assess the performance of these detectors, realistic simulations of data with appropriate spatial and temporal correlation are required. It is of course important to have confidence that the models are sufficiently representative of the real clutter to give reliable predictions of performance. As an example, Fig. 40 shows the performance of a Normalised Adaptive Matched Filter (NAMF) [121], using a covariance estimated by averaging K range cells around the CUT. The figure compares the performance in real clutter compared to simulated performance using model parameters derived from the Ingara data. While the performance is not identical, the trends in both the P_fa variation and detection performance are well reproduced by the model.

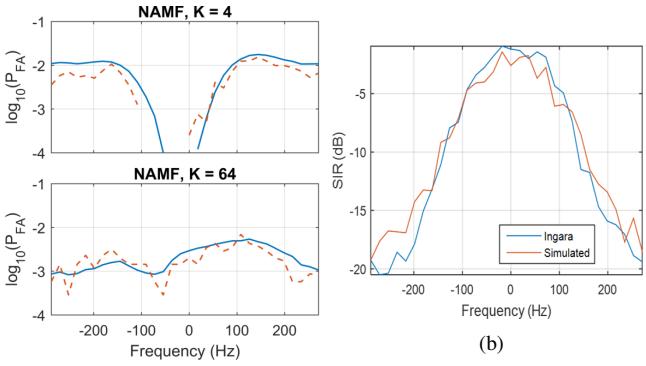

(a) (b)

Fig. 40: Comparison of real and simulated detection performance; (a) P_fa vs. Doppler frequency for $K = 4$ and 64, with a desired P_fa = 10^{-3} [128], (b) Detection performance measured by the signal to interference ratio (SIR) required to achieve $P_\mathrm{d} = 0.5$ and $P_\mathrm{fa} = 10^{-3}$ [130].

VII. Conclusions

Modelling sea clutter requires understanding of the phenomenology and the appropriate statistical models which can be used to represent its characteristics. The first part of this tutorial paper looked at the mean backscatter, amplitude distribution, sea spikes, texture correlation and the Doppler spectrum. To use these models, it is essential to relate the model parameters to the environmental conditions, the collection geometry and the radar frequency and polarisation. Together these models can be used to extrapolate clutter characteristics in unmeasured conditions, accurately simulate sea clutter and to predict the performance of radars with more confidence. The second part of the paper summarised the characteristics of bistatic clutter and how the statistics vary with different bistatic angles. The paper then looked at the application of radar models for clutter simulation and performance prediction for both coherent and non-coherent detection schemes. In all these aspects of maritime radar design, development and testing, it has been demonstrated here that good models of sea clutter are essential.

REFERENCES

[1] K. D. Ward, R. J. A. Tough, and S. Watts, *Sea Clutter: Scattering, the K-Distribution and Radar Performance*, 2nd ed. The Institute of Engineering Technology, 2013.

[2] H. D. Griffiths, W. A. Al-Ashwal, K. D. Ward, R. J. A. Tough, C. J. Baker, and K. Woodbridge, "Measurement and modeling of bistatic radar sea clutter," *IET Radar, Sonar and Navigation*, vol. 4, no. 2, pp. 280–292, 2010.

[3] D. O. Rice, "Reflections of electromagnetic waves from slightly rough surfaces," *Communications on Pure and Applied Maths*, vol. 4, pp. 361–378, 1951.

[4] W. H. Peake, "Theory of radar return from terrain," in *IRE Convention Record*, 1959, pp. 27–41.

[5] J. W. Wright, "Backscattering from capillary waves with application to sea clutter," *IEEE Transactions on Antennas and Propagation*, vol. AP-14, no. 6, pp. 749–754, 1966.

[6] F. T. Ulaby, R. K. Moore, and A. K. Fung, *Microwave Remote Sensing: Active and Passive, Volume II: Radar Remote Sensing and Surface Scattering and Emission Theory*. Addison-Wesley, 1982.

[7] J. W. Wright, "A new model for sea clutter," *IEEE Transactions on Antennas and Propagation*, vol. 16, no. 2, pp. 217–223, 1968.

[8] N. W. Guinard and J. C. Daley, "An experimental study of a sea clutter model," *Proceedings of the IEEE*, vol. 58, pp. 543–550, 1970.

[9] G. R. Valenzuela, M. B. Laing, and J. C. Daley, "Ocean spectra for the high-frequency waves as determined from airborne radar measurements," *Journal of Marine Research*, vol. 29, pp. 69–84, 1971.

[10] F. G. Bass, I. M. Fuks, A. I. Kalmykov, I. E. Ostrovsky, and A. D. Rosenberg, "Very high frequency radiowave scattering by a distributed sea surface, part II: scattering from an actual sea surface," *IEEE Transactions on Antennas and Propagation*, vol. 16, no. 5, pp. 560–568, 1968.

[11] K. Hasselmann and M. Schieler, "Radar backscatter from the sea surface," in *Symposium on Naval Hydrodynamics*, 1970, pp. 361–388.

[12] N. L. Hicks, N. Knable, J. J. Kovaly, G. S. Newell, J. P. Ruina, and C. W. Sherwin, "The spectrum of X-band radiation backscattered from the sea surface," *Journal of Geophysical Research*, vol. 65, no. 3, pp. 825–837, 1960.

[13] D. G. Money, A. Mabogunje, D. Webb, and M. Hooker, "Sea clutter power spectral lineshape measurements," in *IEEE Radar Conference*, 1997.

[14] J. R. Duncan, W. C. Keller, and J. W. Wright, "Fetch and wind speed dependence of Doppler spectra," *Radio Science*, vol. 9, pp. 809–819, 1974.

[15] P. H. Y. Lee, J. D. Barter, K. L. Beach, C. L. Hindman, B. M. Lake, H. Rungaldier, J. C. Shelton, A. B. Williams, R. Yee, and H. C. Yuen, "X-band microwave backscattering from ocean waves," *Journal of Geophysical Research*, vol. 100, no. C2, pp. 2591–2611, 1995.

[16] M. Greco, F. Bordoni, and F. Gini, "X-band sea-clutter nonstationary: influence of long waves," *IEEE Journal of Oceanic Engineering*, vol. 29, no. 2, pp. 269–293, April 2004.

[17] CSIR, "Small boat detection research." [Online]. Available: http://www.csir.co.za/small_boat_detection/

[18] L. Rosenberg and S. Watts, "High grazing angle sea-clutter literature review," DSTO, General Document DSTO-GD-0736, 2013.

[19] L. Rosenberg, "Characterisation of high grazing angle X-band sea-clutter Doppler spectra," *IEEE Transaction on Aerospace and Electronic Systems*, vol. 50, no. 1, pp. 406–417, January 2014.

[20] W. Al-Ashwal, "Measurement and modelling of bistatic sea clutter," Ph.D. dissertation, University College London, 2011.

[21] Weather forecast and reports. [Online]. Available: www.wunderground.com

[22] N. Willis and H. D. Griffiths, *Advances in bistatic radar*. SciTech Publishing, 2007.

[23] L. Rosenberg, D. J. Crisp, and N. J. Stacy, "Analysis of the KK-distribution with medium grazing angle sea-clutter," *IET Proceedings of Radar Sonar and Navigation*, vol. 4, no. 2, pp. 209–222, April 2010.

[24] L. Rosenberg, "Sea-spike detection in high grazing angle X-band sea-clutter," *IEEE Transactions on Geoscience and Remote Sensing*, vol. 51, no. 8, pp. 4556–4562, 2013.

[25] M. A. Ritchie, H. D. Griffiths, S. Watts, and L. Rosenberg, "Statistical comparison of low and high grazing angle sea clutter," in *IEEE International Radar Conference*, 2014.

[26] A. Fiche, S. Angelliaume, and L. Rosenberg, "Analysis of X-band SAR sea-clutter distributions at different grazing angles," *IEEE Transactions of Geoscience and Remote Sensing*, vol. 53, no. 8, pp. 4650–4660, 2015.

[27] S. Watts, L. Rosenberg, S. Bocquet, and M. Ritchie, "The Doppler spectra of medium grazing angle sea clutter; part 1: Characterisation," *IET Radar Sonar and Navigation*, vol. 10, no. 1, pp. 24–31, 2016.

[28] L. Rosenberg and S. Bocquet, "Application of the Pareto plus noise distribution to medium grazing angle sea-clutter," *IEEE Journal of Selected Topics in Applied Earth Observations and Remote Sensing*, vol. 8, no. 1, pp. 255–261, January 2015.

[29] K. McDonald, M. and D. Cerutti-Maori, "Coherent radar processing in sea clutter environments part 1: Modelling and partially adaptive STAP performance," *IEEE Transaction on Aerospace and Electronic Systems*, vol. 52, no. 4, pp. 1797–1817, 2016.

[30] V. Gracheva and J. Ender, "Multichannel analysis and suppression of sea clutter for airborne microwave systems," *IEEE Transactions on Geoscience and Remote Sensing*, vol. 54, no. 4, pp. 2385–2399, 2016.

[31] Z. Guerraou, S. Angelliaume, L. Rosenberg, and C. Gurin, "Investigation of azimuthal variations from X-band medium-grazing-angle sea clutter," *IEEE Transactions of Geoscience and Remote Sensing*, vol. 54, no. 10, pp. 6110–6118, October 2016.

[32] M. McDonald and D. Cerutti-Maori, "Multi-phase centre coherent radar sea clutter modelling and simulation," *IET Radar Sonar and Navigation*, vol. 11, no. 9, p. 13591366, 2017.

[33] M. W. Long, *Radar Reflectivity of Land and Sea - Third Edition*. Artech House, 2001.

[34] F. E. Nathanson, J. P. Reilly, and M. N. Cohen, *Radar Design Principles*, 2nd ed. McGraw-Hill, 1991.

[35] Technology Service Corporation, "Backscatter from sea," *Radar Workstation*, vol. 2, pp. 177–186, 1990.

[36] F. Nathanson and J. Reilly, "Clutter," in *Radar Design Principles: Signal Processing and the Environment*, 2nd ed., F. Nathanson, Ed. SciTech Publishing Inc, 1999, ch. 7, pp. 269 – 349.

[37] S. Bocquet, "Parameter estimation for Pareto and K distributed clutter with noise," *IET Radar Sonar and Navigation*, vol. 9, no. 1, pp. 104–113, 2015.

[38] D. Blacknell and R. J. A. Tough, "Parameter estimation for the K-distribution based on [z log(z)]," *IEE Proceedings of Radar, Sonar and Navigation*, vol. 148, no. 6, pp. 309–312, 2001.

[39] G. V. Trunk and S. F. George, "Detection of targets in non-Gaussian sea clutter," *IEEE Transactions*, vol. AES-6, pp. 620–628, 1978.

[40] P. Fayard and T. R. Field, "Optimal inference of the inverse gamma texture for a compound-Gaussian clutter," in *IEEE International Conference on Acoustics, Speech and Signal Processing*, 2009, pp. 2969–2972.

[41] P. R. Krishnaiah and L. Lin, "Complex elliptically symmetric distributions," *Communications in Statistics - Theory and Methods*, vol. 15, no. 12, pp. 3693–3718, 1986.

[42] E. Ollila, D. E. Tyler, V. Koivunen, and H. V. Poor, "Complex elliptically symmetric distributions: Survey, new results and applications," *IEEE Transactions on Signal Processing*, vol. 60, no. 11, pp. 5597–5625, 2012.

[43] M. Sekine and Y. Mao, *Weibull Radar Clutter*. IEE Radar Sonar and Navigation and Avionics, 1990.

[44] E. Conte, M. Longo, and M. Lops, "Modelling and simulation of non-Rayleigh radar clutter," *IEE Proceedings F*, vol. 138, no. 2, pp. 121–130, 1991.

[45] R. Palamà, M. Greco, P. Stinco, and F. Gini, "Statistical analysis of NetRAD high resolution sea clutter," in *European Signal Processing Conference*, 2013.

[46] K. D. Ward, "Compound representation of high resolution sea clutter," *Electronic Letters*, vol. 17, no. 16, pp. 561–563, 1981.

[47] L. Rosenberg and S. Bocquet, "Non-coherent radar detection performance in medium grazing angle X-band sea-clutter," *IEEE Transactions on Aerospace and Electronic Systems*, vol. 53, no. 2, pp. 669–682, 2017.

[48] A. Balleri, A. Nehorai, and J. Wang, "Maximum likelihood estimation for compound-Gaussian clutter with inverse gamma texture," *IEEE Transactions on Aerospace and Electronic Systems*, vol. 43, no. 2, pp. 775–779, 2007.

[49] M. Farshchian and F. L. Posner, "The Pareto distribution for low grazing angle and high resolution X-band sea clutter," in *IEEE Radar Conference*, 2010, pp. 789–793.

[50] G. V. Weinberg, "Assessing Pareto fit to high-resolution high-grazing-angle sea clutter," *IET Electronic Letters*, vol. 47, no. 8, pp. 516–517, 2011.

[51] Y. Dong, "Distribution of X-band high resolution and high grazing angle sea clutter," DSTO, Research Report DSTO-RR-0316, 2006.

[52] L. Rosenberg, S. Watts, and S. Bocquet, "Application of the K+Rayleigh distribution to high grazing angle sea-clutter," in *International Radar Conference*, 2014.

[53] M. A. Sletten, "Multipath scattering in ultrawide-band radar sea spikes," *IEEE Transactions on Antennas and Propagation*, vol. 46, no. 1, pp. 45–56, 1998.

[54] T. Lamont-Smith, "Translation to the normal distribution for radar clutter," *IEE Proceedings of Radar, Sonar and Navigation*, vol. 147, no. 1, pp. 17–22, 2000.

[55] D. Middleton, "New physical-statistical methods and model for clutter and reverberation: The KA-distribution and related probability structures," *IEEE Journal of Oceanic Engineering*, vol. 24, no. 3, pp. 261–284, 1999.

[56] K. D. Ward and R. J. A. Tough, "Radar detection performance in sea clutter with discrete spikes," in *International Radar Conference*, 2002, pp. 15–17.

[57] W. Watts, K. D. Ward, and R. J. A. Tough, "The physics and modelling of discrete spikes in radar sea clutter," in *International Radar Conference*, 2005, p. 7277.

[58] M. Greco, F. Gini, and M. Rangaswamy, "Statistical analysis of measured polarimetric clutter data at different range resolutions," *IET Proceedings on Radar, Sonar and Navigation*, vol. 153, no. 6, p. 473481, 2006.

[59] D. Walker, "Doppler modelling of radar sea clutter," *IEE Proceedings of Radar, Sonar and Navigation*, vol. 148, no. 2, pp. 73–80, April 2001.

[60] L. Rosenberg and N. J. Stacy, "Analysis of medium angle X-band sea-clutter Doppler spectra," in *IEEE Radarcon Conference*, 2008, pp. 1898–1903.

[61] L. Rosenberg, D. J. Crisp, and N. J. Stacy, "Characterisation of low-PRF X-band sea-clutter Doppler spectra," in *International Radar Conference*, 2008, pp. 100–105.

[62] A. T. Jessup, W. K. Melville, and W. C. Keller, "Breaking waves affecting microwave backscatter, 1. detection and verification," *Journal of Geophysical Research*, vol. 96, no. C11, pp. 20,547–20,559, November 1991.

[63] L. Liu and S. J. Frasier, "Measurement and classification of low-grazing-angle radar sea spikes," *IEEE Transactions on Antennas and Propagation*, vol. 46, no. 1, pp. 27–40, 1998.

[64] H. W. Melief, H. Greidanus, P. van Genderen, and P. Hoogeboom, "Analysis of sea spikes in radar sea clutter data," *IEEE Transactions on Geoscience and Remote Sensing*, vol. 44, no. 4, pp. 985–993, 2006.

[65] D. Walker, "Model and characterisation of radar sea clutter," Ph.D. dissertation, University College London, 2001.

[66] M. Greco, P. Stinco, and F. Gini, "Identification and analysis of sea radar clutter spikes," *IET Journal of Radar, Sonar and Navigation*, vol. 4, no. 2, pp. 239–250, April 2010.

[67] L. B. Wetzel, *Radar Handbook*, 3rd ed. McGraw-Hill, 2008, ch. 15.

[68] P. H. Y. Lee, J. D. Barter, B. M. Lake, and H. R. Thompson, "Lineshape analysis of breaking-wave Doppler spectra," *IEE Proceedings of Radar, Sonar and Navigation*, vol. 145, no. 2, pp. 135–139, 1998.

[69] T. Lamont-Smith, "Investigation of the variability of Doppler spectra with radar frequency and grazing angle," *IEE Proceedings of Radar, Sonar and Navigation*, vol. 151, no. 5, pp. 291–298, 2004.

[70] W. K. Melville, A. D. Rozenberg, and D. C. Quigley, "Laboratory study of polarized microwave scattering at grazing incidence," in *IEEE International Geoscience and Remote Sensing Symposium*, 1995, pp. 951–953.

[71] N. J. S. Stacy, M. Preiss, and D. Crisp, "Polarimetric charactersitics of X-band SAR sea clutter," in *IEEE International Conference on Geoscience and Remote Sensing*, 2006, pp. 4017–4020.

[72] S. Watts, "Modeling and simulation of coherent sea clutter," *IEEE Transactions on Aerospace and Electronic Systems*, vol. 48, no. 4, pp. 3303–3317, October 2012.

[73] G. Davidson, "Simulation of coherent sea clutter," *IET Radar Sonar and Navigation*, vol. 4, no. 2, pp. 168–177, 2010.

[74] M. Ritchie, A. G. Stove, S. Watts, K. Woodbridge, and H. D. Griffiths, "Application of a new sea clutter Doppler model," in *IEEE International Radar Conference*, 2013, pp. 560 – 565.

[75] M. Ritchie, A. Stove, A. Woodbridge, and H. Griffiths, "NetRAD: Monostatic and bistatic sea clutter texture and Doppler spectra characterization at S-band," *IEEE Transactions on Geoscience and Remote Sensing*, vol. 54, no. 9, pp. 5533–5543, September 2016.

[76] S. Watts, L. Rosenberg, S. Bocquet, and M. Ritchie, "The Doppler spectra of medium grazing angle sea clutter; part 2: Exploiting the models," *IET Radar Sonar and Navigation*, vol. 10, no. 1, pp. 32–42, 2016.

[77] S. Bocquet, L. Rosenberg, and S. Watts, "Simulation of coherent sea clutter with inverse gamma texture," in *International Radar Conference, Radar 2014*, October 2014.

[78] S. Kemkemian, L. Lupinski, J. Degurse, V. Corretja, R. Cottron, and S. Watts, "Performance assessment of multi-channel radars using simulated sea clutter," in *International Radar Conference, Radar 2015*, May 2015, pp. 1015–1020.

[79] L. Rosenberg and S. Watts, "Coherent simulation of sea-clutter for a scanning radar," in *NATO SET-239 Workshop on Maritime Radar Surveillance from Medium and High Grazing Angle Platforms*, 2016.

[80] S. Angelliaume, V. Fabbro, G. Soriano, and C. A. Guerin, "The GO-SSA extended model for all-incidence sea clutter modelling," in *IEEE Geoscience and Remote Sensing Symposium*, 2014, pp. 5017–5020.

[81] J. P. Reilly, "Clutter models for shipboard radar applications, 0.5 to 70 GHz, multi-sensor propagation data and clutter modelling," NATO AAW System Program Office, Tech. Rep. F2A-88-0-307R2, NAAW-88-062R2 Technical Report Task 3-1-18, 1998.

[82] I. Antipov, "Simulation of sea clutter returns," DSTO, Technical Report DSTO-TR-0679, June 1998.

[83] V. Gregers-Hansen and R. Mittal, "An improved empirical model for radar sea clutter reflectivity," *IEEE Transaction on Aerospace and Electronic Systems*, vol. 48, no. 4, p. 35123524, 2012.

[84] H. Masuko, K. Okamoto, M. Shimada, and S. Niwa, "Measurement of microwave backscattering signatures of the ocean surface using X band and Ka band airborne scatterometers," *Geophysical Research*, vol. 91, no. C11, pp. 13 065–13 083, 1986.

[85] D. J. Crisp, R. Kyprianou, L. Rosenberg, and N. J. Stacy, "Modelling X-band sea clutter at moderate grazing angles," in *International Radar Conference*, 2008, pp. 596–601.

[86] M. M. Horst, F. B. Dyer, and M. Tuley, "Radar sea clutter model," in *IEEE International Conference of Antennas and Progatation*, no. 169, 1978, pp. 5–10.

[87] L. Rosenberg and S. Watts, "Continuous sea clutter models for the mean backscatter and K-distribution shape," in *International Radar Conference*, 2017.

[88] K. D. Ward, "A radar sea clutter model and its application to performance assessment," in *Internatinal Radar Conference*, 1982, pp. 203–207.

[89] S. Watts and D. C. Wicks, "Empirical models for detection prediction in K-distribution sea clutter," in *IEEE International Radar Conference*, May 1990, pp. 189–194.

[90] L. Rosenberg, D. J. Crisp, and N. J. Stacy, "Statistical models for medium grazing angle X-band sea-clutter," in *Defence Applications of Signal Processing*, 2009.

[91] D. J. Crisp, L. Rosenberg, and N. J. S. Stacy, "Modelling ocean backscatter in the plateau region at X-band with the K-distribution," DST Group, Research report in preparation, 2017.

[92] L. Rosenberg, S. Watts, S. Bocquet, and M. Ritchie, "Characterisation of the Ingara HGA dataset," in *International Radar Conference*, 2015.

[93] R. J. A. Tough and K. D. Ward, "The generation of correlated K-distributed noise," Defence Research Establishment UK, Tech. Rep. DRA/CIS/CBC3/WP94001/2.0, 1994.

[94] H. Griffiths and R. Palamá, *Bistatic clutter modelling*. in Novel radar techniques and applications Vol. 1, IET publishing, 2017, ch. 12.

[95] M. I. Skolnik, *Radar Handbook*, 3rd ed. McGraw-Hill, 2008.

[96] N. J. Willis, *Radar Handbook*, 2nd ed. McGraw-Hill, 1990, ch. 25.

[97] A. Domville, "The bistatic reflection from land and sea of X-band radio waves," GEC-AEI (Electronics) Ltd, Stanmore, UK, Part 1: Memorandum SLM1802, July 1967; Part 2: Memorandum SLM2116, 1968.

[98] W. A. Al-Ashwal, K. Woodbridge, and H. D. Griffiths, "Analysis of bistatic sea clutter - part I: Average reflectivity," *IEEE Transactions on Aerospace and Electronic Systems*, vol. 50, no. 2, pp. 1283–1292, April 2014.

[99] R. Palamà, M. Greco, F. Gini, and P. Stinco, "Statistical analysis of bistatic and monostatic sea clutter," *IEEE Transactions on Aerospace and Electronic Systems*, vol. 51, no. 4, pp. 3036–3054, October 2015.

[100] S. M. Kay, *Fundamentals of Statistical Signal Processing, Estimation Theory, Vol. I*. Prentice Hall PTR, 1993.

[101] R. Palamà, M. Ritchie, H. Griffiths, W. Miceli, F. Fioranelli, S. Sandenbergh, and M. Inggs, "Correlation analysis of simultaneously collected bistatic and monostatic sea clutter," in *IEEE Radar Conference*, 2017, pp. 1466–1471.

[102] F. Posner and K. Gerlach, "Sea spike demographics at high range resolutions and very low grazing angles," in *IEEE Radar Conference*, 2003, pp. 38–45.

[103] R. Palamà, M. Greco, P. Stinco, and F. Gini, "Analysis of sea spikes in NetRAD clutter," in *European Radar Conference*, October 2014, pp. 109–112.

[104] N. J. Willis, *Bistatic Clutter*. SciTech Publishing, 1991.

[105] D. K. Barton, "Land clutter models for radar design and analysis," *Proceedings of the IEEE*, vol. 73, no. 2, pp. 198–204, 1985.

[106] M. W. Long, "On the polarization and the wavelength dependence of sea echo," *IEEE Transactions on Antennas and Propagation*, vol. AP-13, no. 5, pp. 749–754, 1965.

[107] I. Wolfram Research, "Mathematica," 2017.

[108] B. Liu and D. C. Munson, "Generation of random sequences having a jointly specified marginal distribution and autocovariance," *IEEE Transactions on Acoustics, Speech and Signal Processing*, vol. 30, no. 6, pp. 973–983, 1982.

[109] G. L. Wise, A. P. Treganitis, and J. B. Thomas, "The effect of a memoryless non-linearity on the spectrum of a random process," *IEEE Transactions on Information Theory*, vol. 23, no. 1, pp. 84–89, 1977.

[110] R. J. A. Tough and K. D. Ward, "The correlation properties of gamma and other non-Gaussian processes generated by memoryless nonlinear transformation," *Journal of Applied Physics*, vol. 32, pp. 3075–3084, 1999.

[111] C. J. Oliver and R. J. A. Tough, "On the simulation of correlated K-distributed random clutter," *Optica Acta*, vol. 33, p. 223250, 1986.

[112] D. Blacknell, A. Blake, P. Lombardo, and C. J. Oliver, "A comparison of simulation techniques for correlated gamma and K distributed images for SAR applications," in *IEEE International Geoscience and Remote Sensing Symposium*, 1994.

[113] B. C. Armstrong and H. D. Griffiths, "Modelling spatially correlated K-distributed clutter," *Electronic Letters*, vol. 27, no. 15, pp. 1355–1356, July 1991.

[114] S. Watts, "A new method for simulation of coherent sea clutter," in *IEEE Radar Conference*, 2011, pp. 3303–3317.

[115] S. Watts, L. Rosenberg, and M. Ritchie, "Characterising the Doppler spectra of high grazing angle sea clutter," in *International Radar Conference*, 2014.

[116] L. Rosenberg and S. Bocquet, "Robust performance prediction modelling for compound distributions with temporal correlation," in *International Radar Conference*, 2013, pp. 388–393.

[117] P. Swerling, "Probability of detection for fluctuating targets," *IRE Transactions*, vol. IT-6, pp. 269–308, 1960.

[118] ——, "Recent developments in target models for radar detection analysis," in *AGARD Avionics Technical Symposium Proceedings*, Istanbul, Turkey, May 1970.

[119] A. De Maio and M. S. Greco, Eds., *Modern Radar Detection Theory*. SciTech, 2016.

[120] S. Watts and L. Rosenberg, "Coherent radar performance in sea clutter," in *IEEE Radar Conference*, Johannesburg, 2015.

[121] E. Conte, M. Lops, and G. Ricci, "Asymptotically optimum radar detection in compound-Gaussian clutter," *IEEE Transactions on Aerospace and Electronic Systems*, vol. 31, no. 2, pp. 617–625, 1995.

[122] E. Conte, A. De Maio, and G. Ricci, "Covariance matrix estimation for adaptive CFAR detection in compound-gaussian clutter," *IEEE Trans. Aerosp. Electron. Syst.*, vol. 38, no. 2, pp. 415–426, 2002.

[123] F. Gini and M. Greco, "Covariance matrix estimation for CFAR detection in correlated heavy-tailed clutter," *Signal Processing, Special Issue*, vol. 82, no. 12, pp. 1847–1859, 2002.

[124] M. Rangaswamy, "Statistical analysis of the nonhomogeneity detector for non-Gaussian interference backgrounds," *IEEE Transactions on Signal Processing*, vol. 53, no. 6, pp. 2101–2111, June 2005.

[125] O. Besson, S. Bidon, and J.-Y. Tourneret, "Covariance matrix estimation with heterogeneous samples," *IEEE Transactions on Signal Processing*, vol. 56, no. 3, 2008.

[126] M. Greco, P. Stinco, F. Gini, and M. Rangaswamy, "Impact of sea clutter nonstationarity on disturbance covariance matrix estimation and CFAR detector performance," *IEEE Transaction on Aerospace and Electronic Systems*, vol. 46, no. 3, pp. 1502–1513, 2010.

[127] Y. I. Abramovich and O. Besson, "Regularized covariance matrix estimation in complex elliptically symmetric distributions using the expected likelihood approach," *IEEE Transactions on Signal Processing*, vol. 61, no. 23, 2013.

[128] L. Rosenberg and S. Watts, "Coherent detection in medium grazing angle sea-clutter," *IET Radar Sonar and Navigation*, vol. 11, no. 9, pp. 1340–1348, August 2017.

[129] S. Watts, "The effects of covariance matrix mismatch on adaptive CFAR performance," in *International Radar Conference*, September 2013, pp. 324–329.

[130] L. Rosenberg and S. Watts, "Model based coherent detection in medium grazing angle sea-clutter," in *IEEE Radar Conference*, 2016.